Forearc erosion in response to megathrust plate coupling along the Wairarapa Coastline, New Zealand

By
Chantel Jensen

Accepted in Partial Completion
of the Requirements for the Degree
Master of Science

ADVISORY COMMITTEE:

Dr. Colin Amos, Chair

Dr. Allison Pfeiffer

Dr. Isaac Larsen

GRADUATE SCHOOL

David L. Patrick, Dean

MASTER'S THESIS

In presenting this thesis in partial fulfillment of the requirements for a master's degree at Western Washington University, I grant to Western Washington University the non- exclusive royalty-free right to archive, reproduce, distribute, and display the thesis in any and all forms, including electronic format, via any digital library mechanisms maintained by WWU.

I represent and warrant this is my original work and does not infringe or violate any rights of others. I warrant that I have obtained written permissions from the owner of any third party copyrighted material included in these files.

I acknowledge that I retain ownership rights to the copyright of this work, including but not limited to the right to use all or part of this work in future works, such as articles or books.

Library users are granted permission for individual, research and non-commercial reproduction of this work for educational purposes only. Any further digital posting of this document requires specific permission from the author. Any copying or publication of this thesis for commercial purposes, or for financial gain, is not allowed without my written permission.

Chantel Jensen
March 2022

Forearc erosion in response to megathrust plate coupling along the Wairarapa Coastline, New Zealand

A Thesis

Presented to

The Faculty of

Western Washington University

In Partial Fulfillment

Of the Requirements for the Degree

Master of Science

By

Chantel Jensen

March 2022

Abstract

How the subduction zone earthquake cycle contributes to uplift, erosion, and permanent deformation of the overlying forearc remains largely unknown. The Hikurangi subduction zone (HSZ), along the east coast of the North Island of New Zealand, provides a unique location to examine the effects of subduction coupling on forearc deformation over multiple millennia. There, the Wairarapa coastline runs parallel to the HSZ and spans a transitional boundary between locked and freely slipping portions of the plate interface. Using digital topographic analysis and catchment-averaged erosion rates from ^{10}Be in fluvial sands, I examined the geomorphology of the HSZ forearc to evaluate potential connections between plate coupling and forearc erosion and uplift. I calculated basin-averaged metrics including normalized channel steepness (k_{sn}), gradient, relief, and drainage area for 70 fluvial catchments along the Wairarapa coastline and selected nine of those basins for cosmogenic ^{10}Be sampling. I compared these metrics to existing inventories of coastal uplift rates measured from Holocene – Late Pleistocene marine terraces, ranging from 0.3 - 3.7 mm/yr and varying at ~100 km wavelengths. Catchment-averaged erosion rates largely mirror coastal uplift rate and range from 0.5 - 3.4 mm/yr, indicating relatively fast erosion within each of the sampled basins. The highest rates ($\geq$ 2 mm/yr) do not correlate strongly with uplift or other topographic metrics and likely represent delivery of sediment originating below the cosmogenic shielding depth through shallow landsliding or gullying. In general, the greatest relief and steepest channels occur in the Aorangi Range at the southernmost portion of the uplifted forearc. There, basins are formed in the oldest basement greywacke sandstones and lie directly above the locked portion of the megathrust. For basins spanning the entire Wairarapa coast, basin-averaged k_{sn} shows a strong correlation with catchment-averaged slope, relief, and precipitation, but does not correlate as well with coastal

uplift or erosion rate given the range and variability of rock types underpinning coastal basins. Examining these relationships for the Aorangi Range, where the underlying geology is comparatively uniform and plate coupling is strongest, reveals robust, positive correlations between k_{sn}, uplift rate, and erosion rate. The strongly locked region is also where the highest topography, steepest channels, and greatest uplift rates are found. This relationship may indicate that the zone of coupling is stable over geological time and is driving the higher rates of uplift, erosion, and exhumation seen in the Aorangi Range over millennia. My results suggest that subduction coupling is a key driver of long-term forearc erosion and topographic development either through: (1) increased uplift during megathrust earthquakes in the strongly coupled region, or (2) through faster slip on upper plate faults driven by increased stresses from the underlying locked megathrust.

Acknowledgments

I would like to acknowledge the indigenous people of the Ngāti Kahungunu Māori iwi (tribe) to whom the land I study on belongs.

This research was supported by funding from the Western Washington University Graduate School, the Western Washington University Geology department, and the Geological Society of America through the National Science Foundation under Grant Nos. EAR-1759200 and EAR-1759353. Any opinions, findings, and conclusions or recommendations expressed in this material are those of the author(s) and do not necessarily reflect the views of the National Science Foundation. Thanks to the AGeS program for its support. All lidar data used for mapping and topographic analysis were obtained from the Land Information New Zealand (LINZ) or Koordinates databases.

Tēnā koutou (thank you) to my New Zealand collaborators, Dr. Kate Clark, Dr. Nicola Litchfield, and Jaime Delano for providing guidance and collecting samples for me in New Zealand when I could not travel due to pandemic-related restrictions. Similarly, I want to thank Dr. Isaac Larsen and Dr. Brendon Quirk for their assistance preparing, processing, and analyzing my cosmogenic samples and walking me through the process remotely.

Thank you to my labmates Katie Alexander and Jenna Chaffeur for all of the late-night guidance and moral support; I truly would not have made it without you. Thank you to my family, Mom, Dad, Rose, and Ryan for supporting me though this long process even though I know you didn't want me to move all the way to Washington. Mom, you know I couldn't have done it without all of your pep-talks. A big thank you to Nick for the endless moral support and for taking me on adventures to brighten my day whenever I got stressed out. You mean the world to me.

I would like to thank my committee members Dr. Isaac Larsen and Dr. Allison Pfeiffer for their invaluable support, guidance, and feedback. Thank you to my advisor, Dr. Colin Amos for teaching me to work independently and giving me the opportunity to work on such an interesting project. I couldn't have made it through this process without each of you and I thank you for pushing me to be a better scientist.

Table of Contents

List of Tables and Figures

1. Introduction

The geology and geomorphology of subduction zone forearcs record both erosion and uplift over many earthquake cycles, and can be used to evaluate relationships between short-term megathrust deformation and longer-term forearc evolution (e.g., Melnick, et al, 2015; Delano et al., 2017). The short-term, decadal to centennial buildup of elastic strain over repeated earthquake cycles occurs in regions of strong interseismic coupling along the subduction interface, imparting stress on to upper plate faults, ultimately influencing the longer-term evolution of the forearc over multiple millennia (e.g. Savage, 1983; Mazzotti et al., 2000; McCaffrey et al., 2000; Norabuena et al., 2004). Still longer-term subduction related processes such as sediment underplating (e.g. Walcott, 1987; Clift, 2004; von Huene et al., 2004), subduction of thick and buoyant crust (Davy, 1992; Cloos, 1993), and seamount subduction (e.g. Cloos, 1993; Scholz and Small, 1997; Fisher et al., 1998; Dominguez et al., 1998) drive localized and regional uplift and emergence of the overriding plate, typically over millions of years. Because these subduction zone processes operate at varying timescales, they each influence the topography in different ways. Analysis of uplift patterns, deformational wavelengths, and forearc erosion in the overriding plate can help distinguish between these short and long-term processes and can provide insight into which mechanisms are driving long-term forearc evolution (Litchfield et al., 2007).

Subduction zones exhibiting strong interseismic coupling are known to produce the largest and most hazardous earthquakes, and subsequent tsunamis, on Earth (Reyners, 1998). In areas yet to experience a great earthquake historically, our understanding of these events and their associated hazards relies on short-term geodetic measurements of interseismic strain (Wallace et al., 2009; Lindsey et al., 2021) combined with coastal uplift and subsidence studies

(Clark et al., 2019; Nelson et al., 2020). How the earthquake cycle and subduction zone processes contribute to the overall uplift, erosion, and permanent deformation in the overlying forearc, however, remains poorly understood. Links between increased basin-averaged forearc erosion rates and regions of subduction zone uplift have previously been inferred in the southern Cascadia margin of western North America (Balco et al., 2013), although without clear connection to the underlying megathrust earthquake cycle. Increased forearc erosion rates in basins overlying strongly coupled portions of the plate interface may indicate that uplift accrues by repeated coeseismic deformation in these areas. It may also indicate that some component of inelastic strain is retained over multiple earthquake cycles when stress is transferred from the subduction interface and sustained on upper plate faults (Delano et al., 2017, Duckworth et al., 2021). Patterns in forearc basin geomorphology and erosion can highlight the underlying subduction mechanisms that may be influencing surface deformation. When controlled for variations in climate and rock type, basin-averaged erosion rates calculated from concentrations of cosmogenic ^{10}Be in fluvial sediment (Brown et al., 1995; Bierman and Steig, 1996; Granger et al., 1996) can be directly related to variations in rock uplift and normalized channel steepness (k_{sn}) measured from digital terrain models (e.g. Cyr et al., 2010; DiBiase et al., 2010; Wobus et al., 2006). I suggest that basin-averaged erosion rates, coupled with topographic metrics such as k_{sn}, gradient, and relief, can help us differentiate which subduction mechanism is generating permanent deformation across the subduction zone forearc.

The North Island of Aotearoa, New Zealand (Figure 1a) is a unique location to examine how plate coupling and other subduction processes drive uplift and erosion over multiple millennia. There, the Wairarapa coastline parallels the Hikurangi Subduction Zone (HSZ) and overlies a transitional boundary between strongly coupled and uncoupled portions of the plate

interface (Figure 1b) (Wallace et al., 2009). This study uses basin-averaged erosion rates from cosmogenic ^{10}Be in conjunction with high-resolution digital terrain analysis to examine deformational patterns across this transitional boundary. Here, I present new erosion rate measurements along the Wairarapa coastline in New Zealand that build on previous studies of coastal uplift and fluvial incision of the forearc (Litchfield and Berryman, 2005; Litchfield et al., 2007b; Beavan et al., 2012; Litchfield and Clark, 2015). Combined, these data provide insight into short (decadal) and long-term (millennial) subduction zone processes and help to distinguish the main control on forearc evolution. I test whether erosion rates and fluvial basin geomorphology change in concert with variations in subduction zone coupling, or if basin erosion primarily reflects other longer-term drivers.

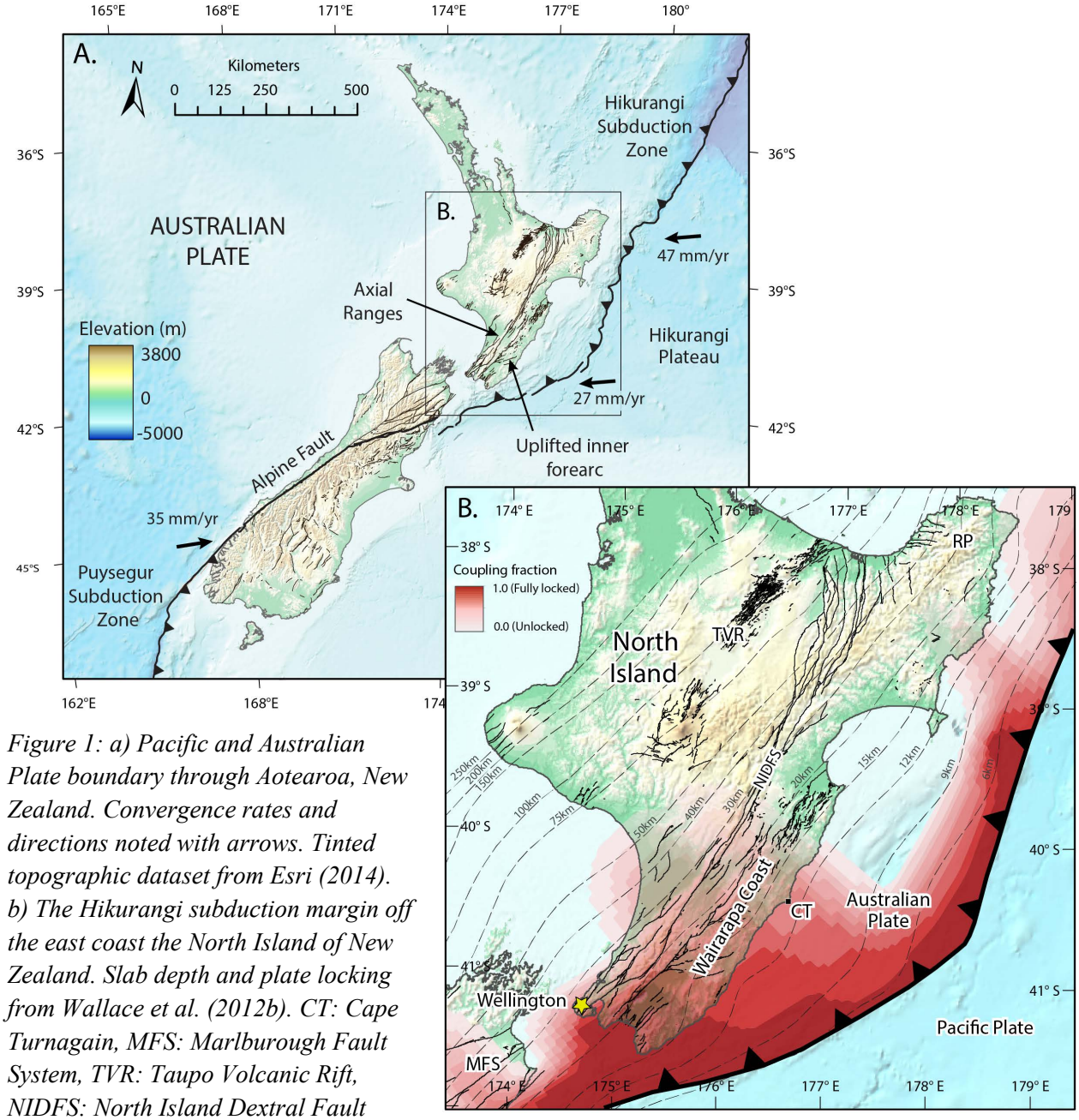

Figure 1: a) Pacific and Australian Plate boundary through Aotearoa, New Zealand. Convergence rates and directions noted with arrows. Tinted topographic dataset from Esri (2014). b) The Hikurangi subduction margin off the east coast the North Island of New Zealand. Slab depth and plate locking from Wallace et al. (2012b). CT: Cape Turnagain, MFS: Marlburough Fault System, TVR: Taupo Volcanic Rift, NIDFS: North Island Dextral Fault System, RP: Raukumara Peninsula.

2. Background

2.1 Tectonic Setting

The Hikurangi Subduction Zone lies offshore to the southeast of the North Island of New Zealand and accommodates oblique southwestward subduction of the oceanic Pacific Plate beneath the continental Australian Plate (Figure 1a). The Pacific and the Australian plates converge at rates between ~20-60 mm/yr over the last ~5 Myr (Nicol and Beavan, 2003), with modern obliquity causing lower relative convergence rates in the south (~27 mm/yr) that increase northward to ~47 mm/yr (Clark et al., 2019). Upper-plate dextral or transpressional faulting, along with the clockwise rotation of the North Island forearc (Wallace, 2004), accommodate the oblique component of subduction on the Hikurangi Subduction Zone (Figure 1b). Over the past ~5 Myr, upper-plate shortening on reverse faults accommodates ~20% of convergent plate motion, while the other ~80% is sustained on the subduction interface (Nicol and Beavan, 2003). Margin-normal shortening is heavily influenced by plate coupling because strongly coupled regions inhibit interplate slip, forcing total convergence (and accumulated interseismic strain) to be absorbed on upper plate faults (Nicol and Beavan, 2003). Although some component of convergent motion is absorbed by shortening in the upper plate, it remains unclear which subduction zone mechanisms (e.g., megathrust earthquakes, triggered slip on upper plate faults, aseismic creep as a result of underplating, imbalanced earthquake cycle, etc.) represent the primary driver on long-term forearc deformation.

2.2 Hikurangi Subduction Zone

The HSZ forearc is largely emergent due to the late Neogene subduction of the anomalously thick and buoyant Hikurangi Plateau (Davy, 1992; Kelsey et al., 1995; Litchfield et al., 2007). The plate interface lies only 10 - 15 km below sections of the North Island due to the

relatively gentle dip (~9°) of the subducting plate (Figure 1b) (Reyners, 1998). The Axial Ranges and uplifted inner forearc each formed in response to the subduction of the Pacific Plate and extend across the eastern North Island (Figure 1b). The Axial Ranges lie 30 km - 70 km inland and directly above the leading edge of the subducting Hikurangi Plateau (Kelsey et al., 1995; Litchfield et al., 2007).

The degree and extent of contemporary interseismic coupling beneath the North Island varies widely along strike of the HSZ (Wallace et al., 2009; Wallace et al., 2012b). The degree of interseismic coupling is calculated from GPS velocities that measure elastic strain rates in the crust in conjunction with fault slip rates (Savage, 1983; Mazzotti et al., 2000; McCaffrey et al., 2000; Norabuena et al., 2004; Wallace et al., 2009; Wallace et al., 2012b). GPS data collected at ~300 sites along the Hikurangi margin show that the downdip termination of coupling is relatively shallow (<15 km) in the north beneath the Raukumara Peninsula with a coupling coefficient of 0.1 - 0.2 (Figure 1b) (Beavan and Haines, 2001; Darby and Beavan, 2001; Wallace, 2004; Wallace et al., 2009; Wallace et al., 2012b). An abrupt transition from weak to strong interseismic coupling exists moving south along the Wairarapa coastline, near Cape Turnagain (Figure 1b). In some locations beneath the southern end of the North Island, the coefficient indicates full interseismic coupling with values between 0.8-1.0 and a downdip extension of ~40 km (Wallace et al., 2009). Strong interseismic coupling causes an accumulation of stresses and often coincides with locations susceptible to major coeseismic strain release in megathrust earthquakes (Wallace et al., 2009). Geological records of past subduction earthquakes can include paleotsunami deposits, submarine turbidities, peat-mud couplets within tidal wetlands (suggesting subsidence), and coastal marine terraces (suggesting uplift). Using these geological signals, Clark et al., (2019) found potential evidence of ten subduction

earthquakes in the last ~7000 years along the Hikurangi margin, with the most recent earthquake occurring ~500BP.

The timing of subduction initiation of the Hikurangi Plateau is contested, with earlier studies suggesting that subduction began 20 - 25 Myr (e.g. Ballance, 1976; Walcott, 1987) and more recent studies suggesting that subduction began 5 Mya (e.g. Furlong and Kamp, 2006). As oceanic crust is subducted along the HSZ, a number of factors beyond interseismic plate coupling, influence deformation and uplift in the overriding Australian plate. Regional morphology and uplift patterns vary widely along the entire margin with uplift rates of 2 - 4 mm/yr in the central and northern Axial Ranges and lower rates of <1 mm/yr along the entire eastern coastline (Litchfield et al., 2007; Beavan et al., 2012). Various deep-seated subduction processes are likely responsible for the observed rock uplift patterns. Potential uplift mechanisms include: sediment subduction/underplating (Walcott, 1987; Clift, 2004; von Huene et al., 2004), relative thickness and buoyancy of the subducting plate (Davy, 1992; Cloos, 1993), presence of fluids (Moore, 1989; Morgan and Karig, 1995), tectonic stress state (Wallace et al., 2009), plate roughness (e.g., seamount subduction) (Cloos, 1993; Scholz and Small, 1997; Fisher et al., 1998; Dominguez et al., 1998), dip of the subducting plate (Davy, 1992; von Huene et al., 2004), and many others (Figure 2). Numerical models conducted by Litchfield et al. (2007) suggest that sediment underplating is the most probable mechanism for higher uplift rates along the Axial

Ranges (Figure 2d), while lower widespread uplift rates are more likely due to the subduction of the anomalously thick and buoyant Hikurangi Plateau (Figure 2f).

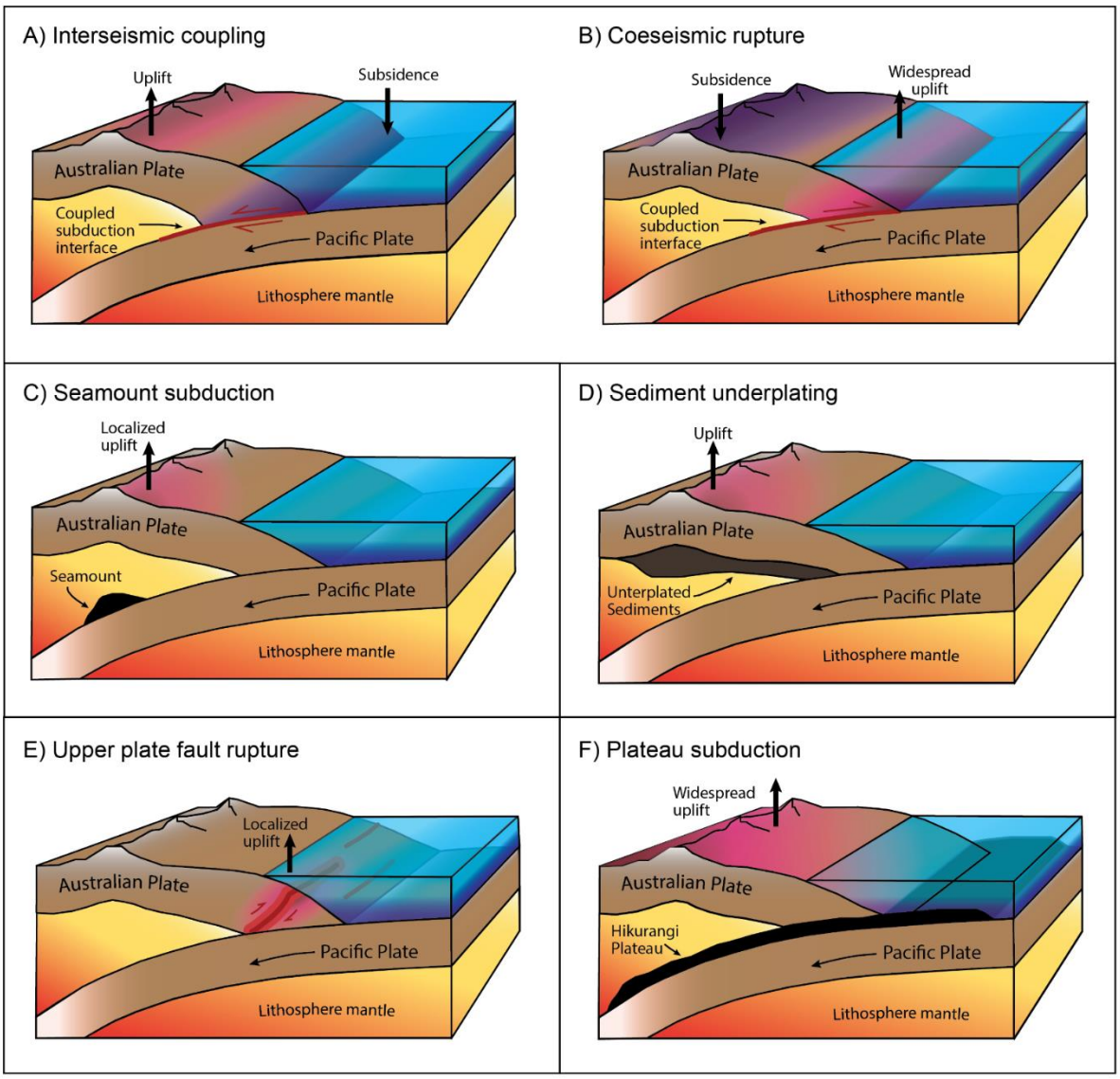

Figure 2: Schematic illustration representing subduction-related processes potentially influencing topographic evolution, and driving rock uplift, in the HSZ forearc. A) and B) Elastic deformation from the interseismic and coeseismic phases of the subduction earthquake cycle, a portion of which may be retained during each seismic cycle, C) Localized aseismic uplift due to seamount subduction, D) Aseismic uplift due to sediment underplating, E) Localized uplift over megathrust splay upper plate fault, F) widespread uplift due to oceanic plateau subduction.

2.3 Forearc Geology

Two primary geologic units underlie the Wairarapa coastline: an upper Jurassic to lower Cretaceous greywacke basement bedrock unit, unconformably overlain by Cretaceous to Tertiary cover sequence (Figure 3a). The basement greywacke bedrock comprises well-indurated,

quartzofeldspathic sandstones and mudstones and are grouped within the lithostratographic unit known as the Torlesse Supergroup. Basement rocks are unconformably overlain by a moderately indurated, Cretaceous to Tertiary cover sequence of the Mangapurupuru and Tinui groups (Lee and Begg, 2002). The Axial and Aorangi Ranges are primarily composed of Triassic to Cretaceous greywacke of the Pahaoa terrane (Lee and Begg, 2002, Lee et al., 2011). Along the coastline, the eastern uplands are predominately composed of Cretaceous to Paleogene sandstones and mudstones of the Waioeka terrane overlain by Neogene sandstones, mudstones, limestones, and conglomerates (Lee and Begg, 2002, Lee et al., 2011). Bedrock ages along the Wairarapa coastline correlate well with rock density (Tenzer et al., 2011), as sedimentary rock density (and strength) is known to increase over time due to lithification and metamorphism (Pfeiffer et al., 2020). The densest units are found in the exposed basement of the Aorangi Range, and the least dense units are present in the northernmost region surrounding Cape Kidnappers (Tenzer et al., 2011).

The Wairarapa coast includes the eastern uplands along the majority of the coastline, and the Aorangi Range at the southernmost point (Figure 3a). The coastal hills of the uplifted inner forearc are primarily drained by east to southeast-flowing rivers sourced throughout the eastern uplands (Lee and Begg, 2002). Range crests in the eastern uplands typically range from 400 m - 500 m elevation, while peaks in the Aorangi Range can reach ~1000 m. Basins in the Aorangi Range are carved in competent, well indurated lower Cretaceous basement sandstone, which forms steep, craggy catchments (Lee and Begg, 2002). East of the Axial Ranges, wide elevated valleys with steep incised hillslopes characterize the upper reaches of the east-flowing coastal drainage basins (Lee and Begg, 2002). Active uplift and sea-level changes heavily influence fluvial aggradation and degradation within the lower reaches of the coastal catchment outlets

(Lee and Begg, 2002; Litchfield and Berryman, 2005; Beavan et al., 2012; Litchfield and Clark, 2015). This change of base-level has created a suite of coastal and fluvial terraces that have been used to distinguish climate vs. tectonic controls on river incision in the North Island (Litchfield and Berryman, 2005; Ninis et al., 2022).

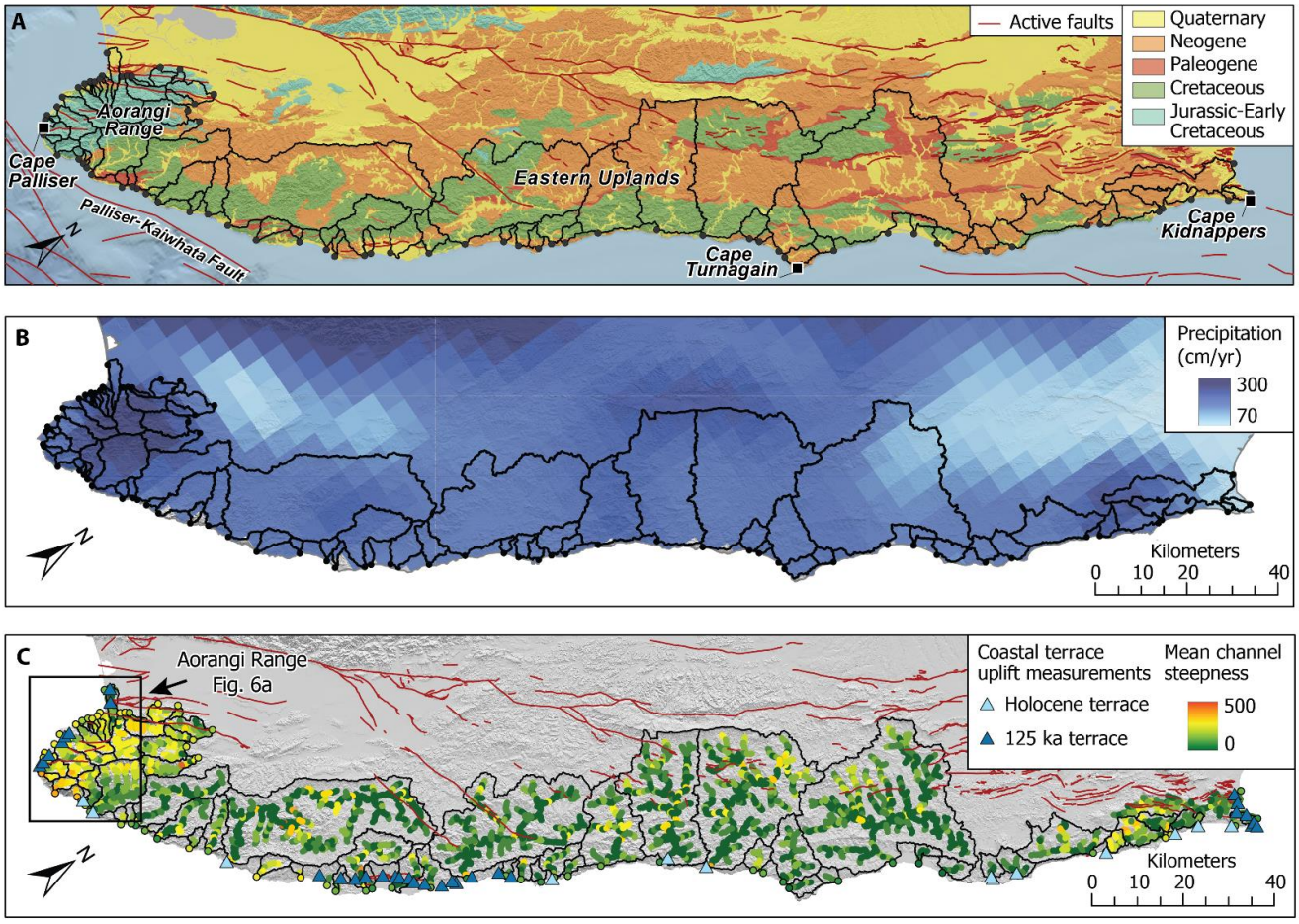

Figure 3: A) Simplified geologic map of the Wairarapa coastline with basin boundaries for reference. Geologic units and bedrock faults are from Begg and Johnston (2000) and Lee and Begg (2002). B) Average annual precipitation map for the years 1972 - 2013. Annual rainfall is estimated from daily rainfall data collected by the National Institute for Water and Atmospheric Research (NIWA), Virtual Climate Station Network (NIWA, 2015). C) Map of Wairarapa coastline; Basins show channel networks colored by normalized channel steepness (k_{sn}). Basin outlets are colored by basin-averaged k_{sn} value. Uplift rate measurements are colored by terrace age and are sourced from Beavan and Litchfield (2012) and N. Litchfield (personal communication, March 2020).

2.4 Upper Plate Faulting

Upper plate faults that splay into the subduction interface have hosted frequent large historical earthquakes independent of megathrust events that produce significant localized coastal uplift. Discontinuous faults can rupture synchronously in variable patterns producing irregular deformation along tens of kilometers of coastline (Clark et al., 2019). Several large upper plate fault earthquakes have been documented along the Wairarapa coastline including the 1855 M_w 8.2 Wairarapa earthquake, 1931 M_w 7.8 Hawkes's Bay Earthquake, and the 1934 M_w 7.6 Pahiatua Earthquake. The 1855 Wairarapa earthquake produced dextral offsets of >18m (Rodgers and Little, 2006) while the 1831 Hawks Bay earthquake produced a maximum uplift of 2.7 m on a blind thrust (Hull, 1990).

The largest fault system in the upper plate, the North Island Dextral Fault System (NIDFS), runs parallel to the Hikurangi Margin through the Axial Ranges, and accommodates a significant portion of the dextral component of plate motion (Figure 1) (Beanland and Haines, 1998). Offshore, the northern region of the Hikurangi margin is characterized by a steeply tapered continental slope while the central margin exhibits a wide accretionary wedge inundated by a series of imbricate reverse faults, including the Palliser-Kaiwhata fault (Figure 3a, S1) (Litchfield et al., 2007). Just south of Cape Palliser, through the Cook Straight, the southern Hikurangi margin transitions back to a narrow continental slope with predominantly strike-slip faulting as plate motion is transferred onto the Marlborough Fault System and Alpine Fault of the South Island (Figure 1a) (Clark et al., 2019). Throughout the offshore transitional zone, plate motion is transferred from the HSZ to the Alpine fault, where there are discontinuous east-northeast trending compressional faults separating small basins in the Cook Straight (Begg and Johnstn, 2000; Clark et al., 2019).

West-dipping reverse faults and monoclines are characteristic of the eastern uplands including the Wairangi/Ngapotiki Fault that runs through the Aorangi Range (Begg and Johnston, 2000) (Figure S1). The onshore reverse faults in the uplifted forearc show no active displacement since the Pliocene-early Quaternary, while the faults more recently active in the late Quaternary are dominantly dextral strike-slip (Lee and Begg, 2002). The temporal transition of onshore faults from thrust to strike-slip, suggests modern-day strain partitioning is being heavily influenced by clockwise rotation of the southern Hikurangi forearc (Kelsey et al., 1995; Lee and Begg, 2002). From the Pliocene to the Pleistocene the southern forearc has exhibited evidence of ~10° clockwise rotation that is likely a result of oblique convergence along the accretionary wedge (Kelsey et al., 1995; Lee and Begg, 2002).

2.5 Coastal Uplift Rates

Holocene marine terraces are present along much of the central Hikurangi margin, while older, Pleistocene terraces are found intermittently along the coastline. The uplift rate dataset used for this study was originally published by Beavan and Litchfield, (2012), but has since been updated to include more data (N. Litchfield, personal communication, March 2020). The database represents a comprehensive inventory of all coastal terrace uplift rates published in New Zealand and includes uplift rates calculated from both the Holocene marine terraces (light blue triangles on Figures 3c and 4c) and the older 125,000 ka Pleistocene terraces (dark blue triangles on Figures 3c and 4c), which coincide with the last interglaciation period. Because the terrace uplift data do not perfectly align spatially with the basin outlets, I projected the terrace uplift data to a coast parallel profile and interpolated the data using a 10^{th} order polynomial (Figure 4c). Uplift rate values were then inferred at the outlet of each basin (Table S1).

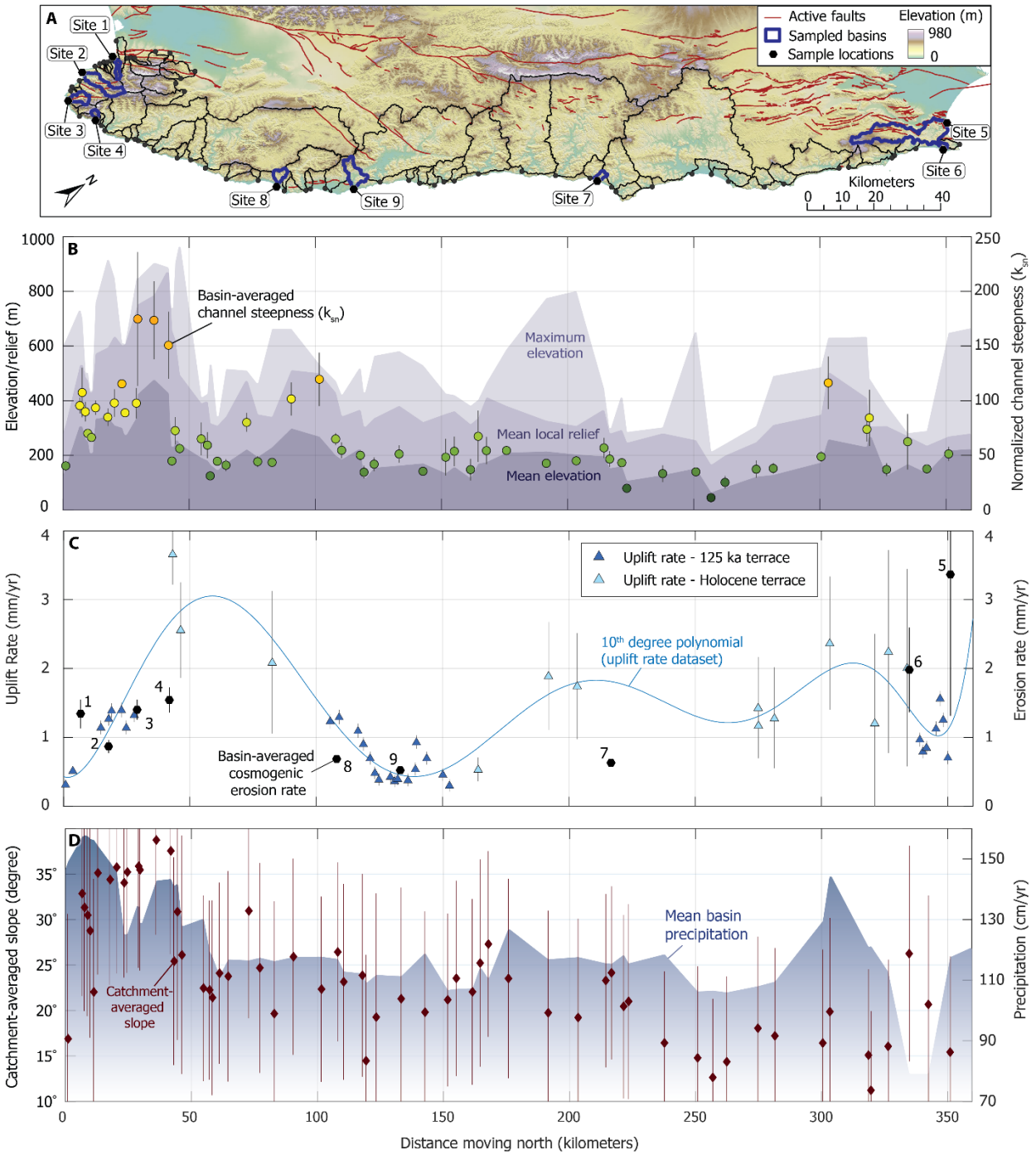

Figure 4: A) Elevation map of the Wairarapa coastline with basin boundaries and sample locations highlighting the spatial distribution of the nine basins selected for ^{10}Be cosmogenic erosion analysis. B) Coast-parallel profile presenting basin-averaged k_{sn} (colors correspond to basin outlets in Figure 3c), basin-averaged relief, maximum elevation, and minimum elevation. C) Coast-parallel profile of coastal uplift rate and basin-averaged cosmogenic erosion rate. Marine terrace uplift rate dataset from Beavan and Litchfield (2012) and N. Litchfield (personal communication, March 2020). D) Coast-parallel profile of catchment-averaged slope and precipitation. Annual rainfall is estimated from daily rainfall data collected by the collected by the National Institute for Water and Atmospheric Research (NIWA), Virtual Climate Station Network (NIWA, 2015).

3. Methods

I used topographic analysis of digital elevation data and basin-averaged erosion rate measurements from cosmogenic radionuclides to evaluate how erosion rate and the geomorphology of the Wairarapa coast varies as a function of the proposed uplift mechanisms.

3.1 Digital Topographic Analysis

Basin-averaged metrics such as channel steepness (k_{sn}), relief, drainage area, precipitation, and coupling, are used to quantify channel network topology. With freely available high-resolution digital topographic data accessed through the Koordinates geospatial data platform, I mapped and characterized 70 basins spanning the Wairarapa coastline. Other software utilized for data visualization includes the Topographic Analysis Kit (TAK) (Forte and Whipple, 2019) and ArcGIS Pro (Esri Inc., 2021).

The Topographic Analysis Kit (TAK) is a Matlab toolkit that calculates basin-averaged statistics including normalized channel steepness, concavity, gradient, relief, elevation, and drainage area, along with many other metrics (Forte and Whipple, 2019). I used the TAK in conjunction with TopoToolbox (Schwanghart and Kuhn, 2010; Schwanghart and Scherler, 2014) to generate longitudinal stream profiles and maps of catchment-averaged metrics in order to identify areas where higher values of channel steepness, relief, etc. may indicate higher values of rock uplift rate. For input into the TAK, I used the 15-meter NZSoSDEM v1.0 digital elevation model (DEM), publicly available from the Koordinates database (koordinates.com). This DEM covers the entire North Island and was created by the University of Otago, School of Surveying through interpolation of topographic vector data from the Topo250 topographic map series (Columbus et al., 2011). After inputting the 15-meter DEM into the TAK, I created a stream network with a minimum threshold drainage area of 5 km^2 (Figure 3c). In later iterations I

lowered the minimum threshold drainage area to 1 km^2 for select areas near Cape Palliser and Cape Kidnappers to include smaller basins in the higher relief ranges. Standard protocols in the TAK workflow included selecting threshold drainage area, choosing basins with coastal outlets, and computing basin-averaged and channel profile statistics (Table S1). I used ArcGIS Pro in conjunction with several supplemental datasets to calculate basin-averaged statistics not available through the TAK. These supplemental datasets include average basin precipitation (Figure 3b) (NIWA, 2015), interseismic coupling along the plate interface (Figure 1b) (Wallace et al., 2012b), and underlying geology (Figure 3a) (Begg and Johnston, 2000; Lee and Begg, 2002). Once basin-averaged statistics were calculated, certain metrics were plotted against each other to identify correlations, and on coast parallel profiles to identify patterns along strike of the subduction zone (Figure 4).

Normalized Channel Steepness

Topographic data collected from fluvial and bedrock channels in varying settings reveal a scaling between channel slope and the contributing upstream drainage area (Duvall et al., 2004; Wobus et al., 2006; Duvall et al., 2019). This relationship can be represented by the equation:

$$S = k_s A^{-\theta} \quad (1)$$

where S = local channel slope, k_s = channel steepness, A = contributing upstream drainage area, and θ = channel concavity. Previous studies have documented the influence of uplift rate on the channel steepness and concavity indices (e.g., Kirby and Whipple, 2001; Duvall et al., 2004; Cyr et al., 2010; Duvall et al., 2019), where high channel steepness values can indicate increased tectonic uplift rates and variations in steepness within a single channel profile can influence channel concavity (Duvall et al., 2004). A normalized channel steepness (k_{sn}) value is based on a single reference concavity (from the mean of observed concavity values), and is frequently used

when comparing channels of different concavities (Sklar and Dietrich, 1998; Wobus et al., 2006). Although channel steepness and concavity can provide a proxy for local uplift rate, it is important to consider other factors including climatic and lithologic variations on the channel profile (Duvall et al., 2004; Duvall et al., 2019).

For this study, normalized channel steepness values were calculated along the stream network using the TAK *KsnChiBatch* function which is calculated for individual channel segments using equation 1. Basin-averaged normalized channel steepness values and their associated standard error values were calculated after running the TAK *ProcessRiverBasins* function and are noted on Table S1.

Catchment-mean local relief and slope

Local relief is calculated as the difference between maximum and minimum elevation values within a specified radius and can be averaged across the catchment. Using the TAK *ProcessRiverBasins* function in conjunction with the *calc_relief* optional input, I calculated relief using a 2.5 km radius moving window, which was then averaged for each basin. Additionally, slope is calculated as a statistical output through the Esri ArcPro *Slope* tool using a 3x3 cell moving window which is then averaged across the basin.

3.2 Cosmogenic Nuclide Erosion Rate Analysis

We chose nine river basins for measurement of *in situ*-produced ^{10}Be concentrations along the Wairarapa coastline (Figure 4a) that rage in size from 4 to 120 km^2 and can be divided into three subgroups: southern Aorangi Range (sites 1 - 4), northern Cape Kidnappers (sites 5 and 6), and central Wairarapa (sites 7, 8, and 9). Basins were selected to span the observed range of uplift rates, coupling, and channel steepness values. Although the predominant rock types along the Wairarapa coastline are sandstones and mudstones, which contain quartz suitable for

cosmogenic ^{10}Be analysis, I was careful to select basins with a high percentage of quartz-rich sandstone that is uniformly distributed throughout the catchment (Lee and Begg, 2002). To further control for rock type, I sampled four basins in the Aorangi Range, where the entirety of the catchment is underlain by a single basement bedrock unit. For each of the nine basins, approximately 3 - 5 kilograms of river sediment was wet-sieved in the field to the 250 - 850 μm grain size. Samples were collected from surfaces of in-channel deposits or bars deposited by recent flows as these locations are frequently replenished with well-mixed fluvial river sediment, providing a temporal representation of upstream eroded materials.

^{10}Be Geochemistry

Cosmogenic nuclides, such as ^{10}Be, ^{36}Cl, and ^{26}Al, are created as cosmic rays propagate through the atmosphere and collide with minerals in rock at the surface of the Earth (Figure S2) (Lal, 1991). Because ^{10}Be is radioactive (half-life = 1.39 Ma), it is essentially nonexistent in rock before it is exposed to cosmic rays, making it an ideal isotope for basin-scale erosional studies (von Blanckenburg, 2006). For this study, ^{10}Be was extracted from quartz, which is abundant in silicate rocks such as the greywacke along the Wairarapa coastline, and is resistant to physical and chemical erosion (von Blanckenburg, 2006). Cosmogenic nuclides are only produced in the upper few meters of rock and soil and accumulate over time at a steady rate (Lal, 1988; Bierman and Steig, 1996). As soil and rock become exposed due to erosion of the overlying layers, accumulation of the *in-situ* isotopes begins (Figure S2). Depending on the rates of denudation, material will have an increasing concentration of radionuclides, proportional to the duration of exposure (Brown et al., 1995; Bierman and Steig, 1996; Granger et al., 1996). Because of this relationship, the concentration of *in-situ* ^{10}Be in river sediment samples is inversely proportional to the basin-averaged erosion rate (Brown et al., 1995; Bierman and Steig, 1996; Granger et al.,

1996). Basins that erode more rapidly will have a low concentration of ^{10}Be in fluvial sediment while basins that erode more slowly will have higher concentrations of ^{10}Be in fluvial sediment (Brown et al., 1995; Bierman and Steig, 1996; Granger et al., 1996).

The ^{10}Be sediment samples underwent physical and chemical preparation at the University of Massachusetts Cosmogenic Nuclide Laboratory. Samples were sieved to isolate the target grain size fraction of 250 - 850 μm and subsequently passed through a magnetic roll separator to isolate non-magnetic grains. Quartz in the non-magnetic fraction was confirmed to be mono-mineralic, so no further crushing was needed. The non-magnetic fraction was pre-treated by leaching with hot, dilute hydrochloric acid followed by leaching in a heated solution of sodium hydroxide and hydrogen peroxide. Pure quartz separates were generated by several, week-long etches in a heated ultrasonic bath using 2% hydrogen fluoride. Quartz purity was assessed by ICP-OES (inductively coupled plasma - optical emission spectrometry) measurement of aluminum following standard procedures outlined in Kohl and Nishiizumi (1992). After addition of ~250 μg of Be carrier, the quartz was dissolved and beryllium was chemically separated. The samples were then forwarded to the Center for Accelerator Mass Spectrometry at Lawrence Livermore National Laboratory where ^{10}Be/^{9}Be ratios were measured.

Erosion Rate Calculation

I used the CRONUS-Earth online calculator (http://hess.ess.washington.edu) version 3 and computational techniques described in Balco et al. (2008) to interpret ^{10}Be concentrations as catchment-averaged erosion rates. The rates account for both physical and chemical erosion of bedrock. I calculated ^{10}Be production rate parameters, including the average basin effective atmospheric pressure, from catchment hypsometry (Portenga and Bierman, 2011) for input into the online calculator. Erosion rates are reported using the St latitude-altitude scaling factor along

with the internal, primarily analytical, uncertainties (Table 1). Denudation rates were also confirmed using a second method: the Basinga GIS toolbox (Charreau et al., 2019). Basinga is an ArcMap compatible extension that can compute basin-averaged cosmogenic production and denudation rates using a digital elevation model (Charreau et al., 2019) (Table 1).

4. Results

4.1 Fluvial basin topography along the Wairarapa coastline

The basin-averaged metrics calculated for this study include uplift, precipitation, coupling, and various topographic metrics such as k_{sn}, slope, and relief (Table S1). In general, normalized channel steepness is highest in high-relief areas where there are large changes in slope moving downstream (Figure 3c and 4b). Basin-averaged normalized channel steepness exhibits a steady increase and peak in the southern Aorangi Range with $k_{sn} > 170$, followed by a dramatic drop to $k_{sn} < 50$ and small fluctuations moving north (Figure 4b). Likewise, there is a comparable, steady increase and peak in uplift rate in the Aorangi Range followed by a similar prominent dip. This pattern of uplift rates is highlighted in the 10^{th} order polynomial plotted through the coast-parallel profile uplift dataset on Figure 4c. Catchment-averaged slope is greatest is the highest relief basins found in the southern Wairarapa (Figure 4d). Precipitation follows a similar pattern, albeit with larger fluctuations in the northern coast near Cape Kidnappers (Figure 4d).

When catchment-mean k_{sn} is plotted against other basin-averaged metrics the strongest correlations are noted with relief ($R^2 = 0.7$) and slope ($R^2 = 0.5$) (Figures 5a and b), followed by a slightly weaker correlation with precipitation ($R^2 = 0.3$) (Figure 5c). It is important to note that relief, slope, and precipitation are inherently linked. There is also a relatively weak correlation with coupling ($R^2 = 0.1$) (Figure 5d). No strong correlation exists between k_{sn} and uplift rate (R^2

= 0.02) when observing the entire dataset as a whole (Figure 5e). To explore this lack of correlation, I chose to narrow our dataset to a region of uniform underling lithology to better control for differences in rock type.

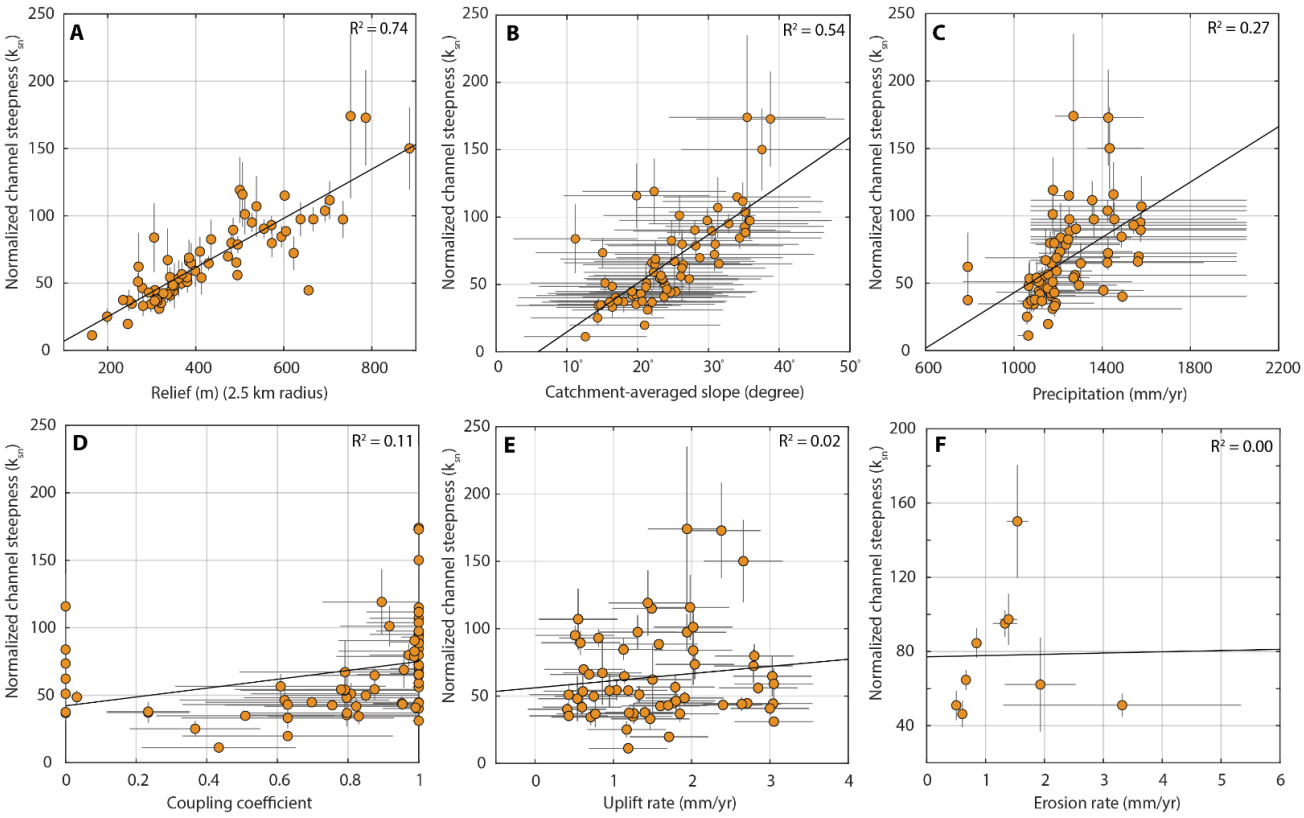

Figure 5: Basin-averaged normalized channel steepness (k_{sn}) plotted against other basin-averaged metrics using the complete dataset of 70 basins along the Wairarapa coastline. Exact values and their associated error can be found on Table S1.

4.2 Normalized channel steepness (k_{sn}) in the Aorangi Range

We evaluated a subset of data in the Aorangi Range to remove the effects of variable rock type on channel steepness. Many basins along the Wairarapa coastline are underlain by a mixed lithology of Cretaceous to Tertiary sandstones and mudstones. Out of the 70 total basins analyzed in this study, there are nine basins in the Aorangi Range (Figure 6a) that are dominantly underlain by a single geologic unit: the Jurassic to lower Cretaceous Pahau Terrane Sandstone.

After narrowing the dataset to the nine basins that are primarily underlain by this single geologic unit, a substantially stronger correlation between uplift rate and channel steepness ($R^2 = 0.5$) is revealed (Figure 6b).

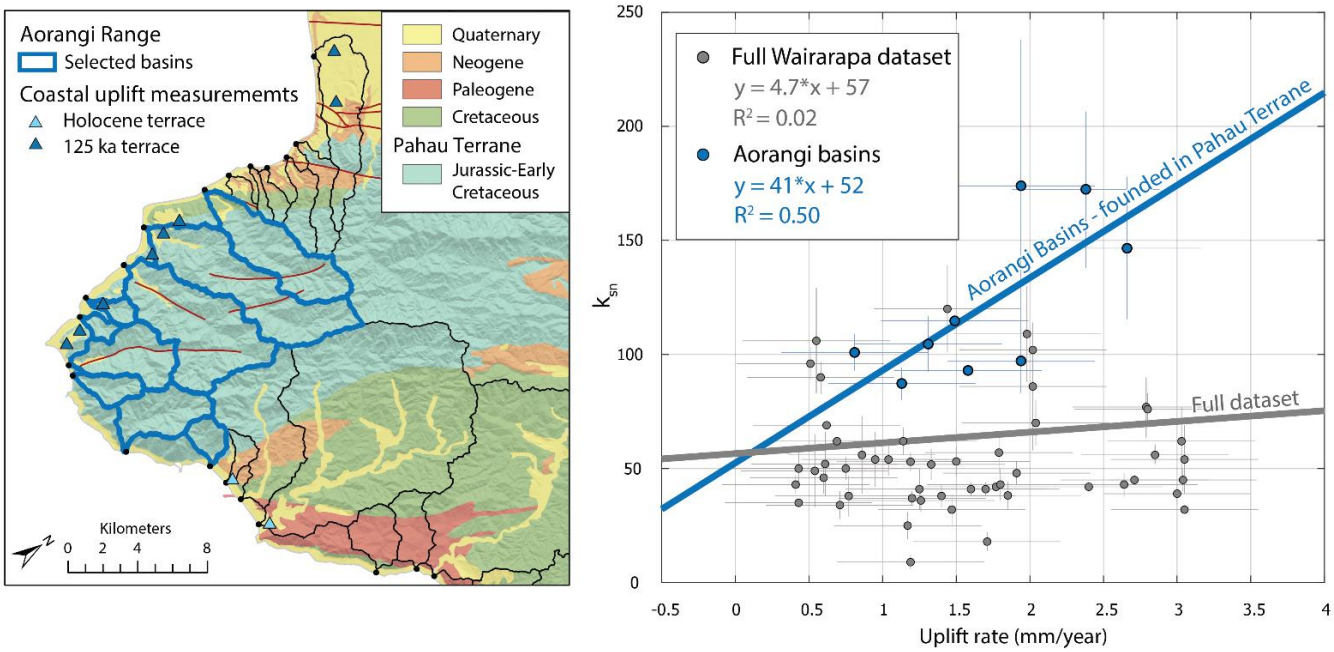

Figure 6: Selected basins are predominantly underlain by the Jurassic to lower Cretaceous Pahau Terrane Sandstone basement bedrock unit. a) (left) Map showing locations of selected basins in the Aorangi Range (outlined in blue) relative to larger dataset. See Figure 3c for extent indicator. b) (right) Plot of k_{sn} vs. uplift rate comparing the full Wairarapa dataset (gray) against the Aorangi dataset (blue).

In basins where fluvial channels traverse from the denser, upper Jurassic to lower Cretaceous basement bedrock units into the less dense mixed lithology sequence, normalized channel steepness values are strikingly different. The k_{sn} values are noticeably higher in channels formed in older basement units like the Pahau Terrane, where the sandstones form steep valley walls and relatively small drainage basins. As the channels transition into younger overlying bedrock and cover sequences, there is a dramatic drop in channel steepness. Figure 7 highlights these differences by comparing the channel steepness values in different rock types.

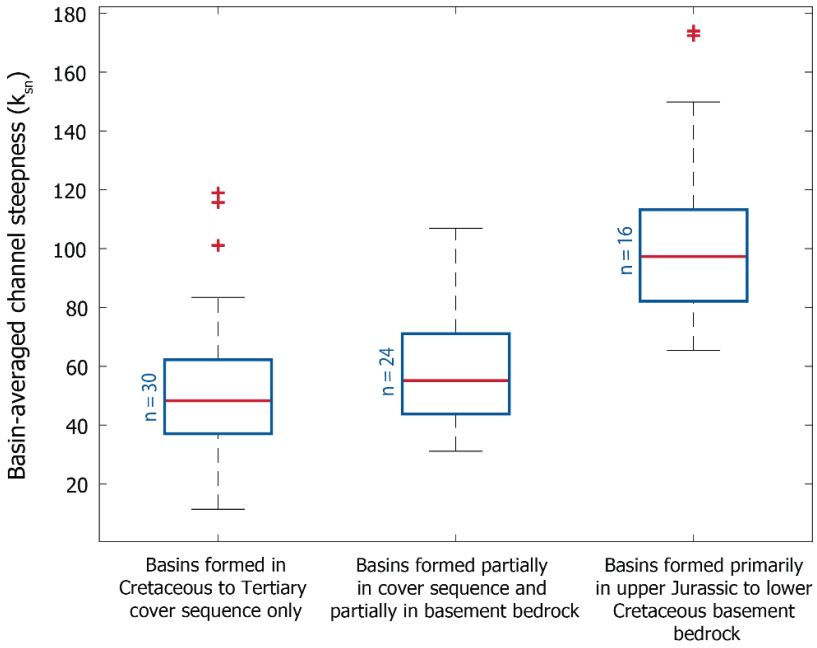

Figure 7: Box-and-whisker plot showing the relative differences in channel steepness between basins founded in cover sequence only, basement bedrock only, and basins that have a mixture of basement and cover sequence. Note that the basins founded predominantly in the basement units have the highest channel steepness (k_{sn}) values.

4.3 Erosion Rates

Overall, ^{10}Be concentrations are very low among the nine samples (Table 1), indicating relatively rapid erosion within each of the sampled basins (Figure 4a). Apparent basin-averaged erosion rates are consistent between different calculation methods and range from 0.5 - 3.4 mm/yr (Figure 4c). In general, calculated erosion rates are consistent within each of the three subregions (northern, central, southern), with the highest apparent erosion rates present in the northern basins of Cape Kidnappers (sites 5 and 6). There, calculated rates range from 2 - 3.4 mm/yr. It is important to note that the highest erosion rates typically correspond to samples with very low ^{10}Be concentrations, thus leading to higher uncertainties at these sites. The lowest erosion rates were found in the central Wairarapa basins (sites 7, 8 and 9) ranging from 0.5 - 0.7 mm/yr. The southern Aorangi Range basins showed moderately high erosion rates ranging from 0.9 - 1.6 mm/yr. Integrating these erosion rates over one or two *e*-folding apparent attenuation

lengths (~60 cm) (Dunai, 2010; Gosse and Phillips, 2001) suggests that our measurements record fluvial erosion over one or more millennia in the central Wairarapa.

Table 1. Cosmogenic erosion rate data and local rock uplift rates along the Wairarapa coastline, NZ

*Basin River Name**	*Site number*	*Location[†] (DD °N/°E)*	*Atmospheric pressure[§] (hPa)*	*^{10}Be [#] (10^2 at/g quartz)*	*Erosion rate** (mm/yr)*	*BASINGA Erosion rate[††] (mm/yr)*	*Uplift Rate[§§] (mm/yr)*
Aorangi Range (South)							
Hurupi Stream	Site 1	-41.436973/175.248921	975.6	29.9 ± 4.6	1.35 ± 0.21	1.16 ± 0.19	0.51 ± 0.5
Pararaki Stream	Site 2	-41.494926/175.266101	972.2	47.3 ± 5.2	0.87 ± 0.10	0.70 ± 0.09	1.13 ± 0.5
Mangatoetoe Stream	Site 3	-41.566055/175.260343	972.3	29.2 ± 3.0	1.41 ± 0.15	1.15 ± 0.14	1.94 ± 0.5
Waiarakeke Stream	Site 4	-41.557333/175.332293	961.1	28.6 ± 3.4	1.55 ± 0.18	1.21 ± 0.16	2.66 ± 0.5
Cape Kidnappers (North)							
Maraetotara River	Site 5	-39.747145/176.943669	987.7	11.0 ± 6.7	3.38 ± 2.06	3.01 ± 1.84	1.33 ± 0.5
Unnamed (Rangaiika)	Site 6	-39.690456/177.055924	994.2	18.0 ± 5.6	1.99 ± 0.62	2.17 ± 0.67	1.50 ± 0.5
Central Wairarapa							
Papuka Stream	Site 7	-40.508196/176.482712	995.1	56.1 ± 5.0	0.64 ± 0.06	0.70 ± 0.08	1.80 ± 0.5
Arawhata Stream	Site 8	-41.234507/175.860968	989.8	53.5 ± 3.4	0.70 ± 0.04	0.71 ± 0.06	1.14 ± 0.5
Motuwaireka Stream	Site 9	-41.081279/176.027318	1011.8	61.3 ± 6.9	0.53 ± 0.06	0.68 ± 0.09	0.43 ± 0.5

*River names are based on the cartographic text shown on NZ Topo50 maps as of December 2021. Source: LINZ database (https://data.linz.govt.nz).

[†]Latitude/longitude are in decimal degree, based on the NZGD2000 datum.

[§]Average basin effective atmospheric pressure determined from catchment hypsometry (Portenga and Bierman, 2011) and based on the constant production rate model (Lal, 1991; Stone, 2000).

[#] [^{10}Be] measured by accelerator mass spectrometry at Center for Accelerator Mass Spectrometry at Lawrence Livermore National Laboratory, against standards prepared by K. Nishiizumi.

** Erosion rates calculated using the CRONUS-Earth online calculator (http://hess.ess.washington.edu) version 3 (Balco et al., 2008), and St latitude-altitude scaling factor. Quoted uncertainty is the internal (analytical) uncertainty.

[††] Erosion Rates calculated using the 'BASINGA' ArcMap extension, (Charreau et al., 2019).

[§§]Uplift measurements calculated using Beavan and Litchfield (2012) data compilation and N. Litchfield (personal communication, March 2020). Quoted uncertainty of ± 0.5 is a midway value between the full dataset's standard deviation (0.73) and the average uplift uncertainty (0.34).

Moving from south to north along the Wairarapa coastline, erosion rates are relatively consistent with subduction coupling along the Hikurangi interface (i.e. decreasing), until the northernmost sites at Cape Kidnappers where apparent erosion rates peak (Figure 4a, c). To better understand this pattern, I plotted basin-averaged erosion rates against several other basin-averaged metrics including coupling, relief, normalized channel steepness, slope, precipitation, and uplift rate (Figure 8).

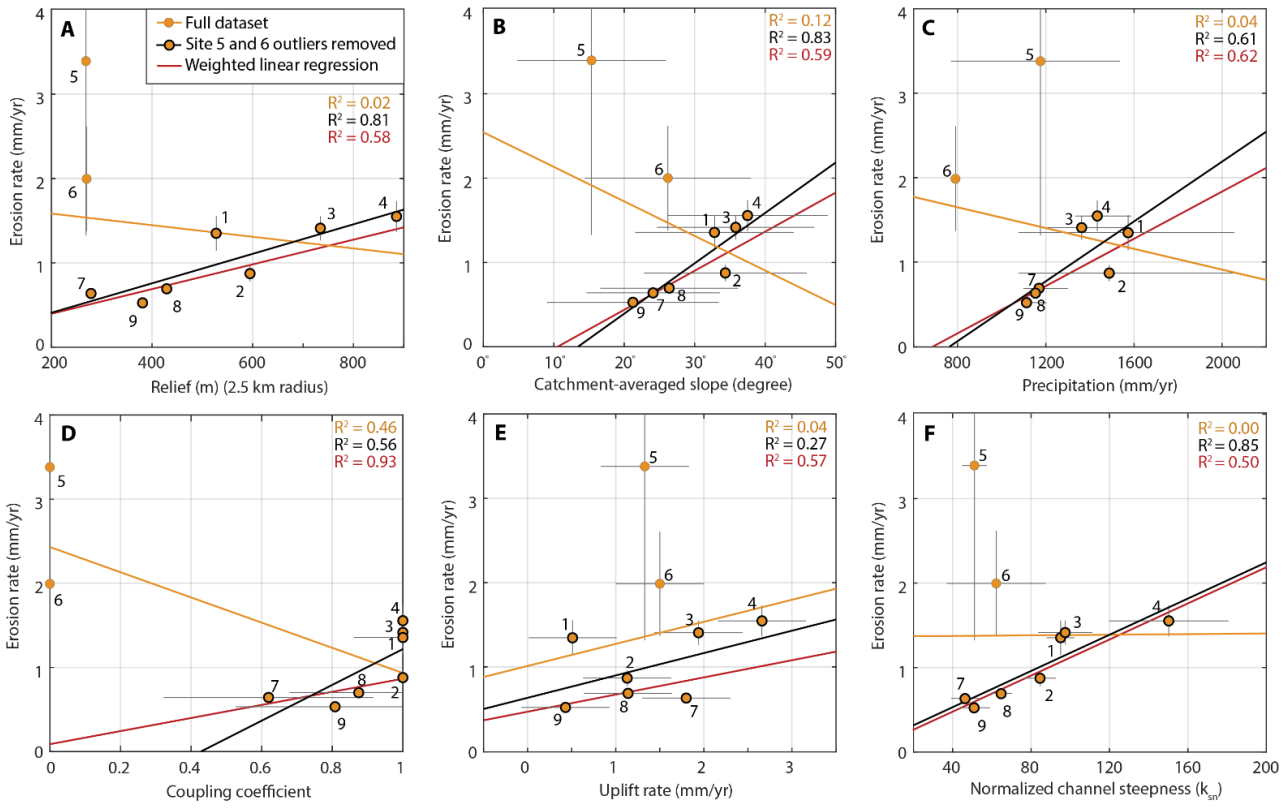

Figure 8: Basin-averaged erosion rate plotted against other basin-averaged metrics. The orange trend line represents the full dataset of all nine basins. The red line is a weighted linear regression providing more weight to the basins with less erosion rate error, and less weight to the basins with large erosion rate error. The black trend line represents the dataset when sites 5 and 6 are removed altogether.

Including the entire dataset reveals poor correlation between erosion rate and all other metrics (orange trendlines on Figure 8). This is due to the very low ^{10}Be concentrations and subsequent high calculated erosion rates for the Cape Kidnappers basins, which otherwise have very low relief, slope, and channel steepness. Using an error-weighted regression results in a higher correlation coefficient between erosion rate and all other measured metrics (coupling, relief, normalized channel steepness, slope, precipitation, and uplift rate), and is highlighted by the red trendlines on Figure 8. This strong correlation can also be seen if sites 5 and 6 are removed altogether (see discussion below). In particular, once sites 5 and 6 are given less weight

or removed, we see the strongest positive correlations with coupling, relief, and channel steepness. The weaker correlations are found with slope, precipitation, and uplift rate. Excluding erosion rate, the highest values for all basin-averaged statistics were found in the Aorangi Range of the southern Wairarapa (sites 1 - 4). Conversely, the lowest basin-averaged statistics came from basins in the central Wairarapa (sites 7 - 9) or northern Cape Kidnappers (sites 5 and 6).

5. Discussion

Implications of bedrock erodibility on topography

Catchment foundation lithology plays a significant role in forearc topography regardless of external tectonic forcing (Allen et al., 2013; Duvall et al., 2004; Miller, 2015). Bedrock competency has been found to strongly influence incision rate and subsequently, channel concavity and steepness (Sklar and Dietrich, 2008; Duvall et al., 2004). In general, channels eroded into competent basement bedrock are steeper and higher relief (i.e. Aorangi Range) while channels flowing through the younger, less dense, sedimentary cover sequence are typically less steep, and lower relief (Figures 3a and 4b). Basins of increased relief are typically linked to increased sediment flux, and consequently, increased erosion rates in tectonically active mountain ranges (Ahnert, 1970; Montgomery and Brandon, 2002). When spatial variability in bedrock strength is compounded with variability in tectonic forcing, it can be difficult to distinguish the dominant drivers of basin morphology. Thus, separating the effects of rock type from these vertical forcings is only possible by comparing basins within a single rock type. The relationships highlighted in Figures 6 and 7 demonstrate that channel steepness is strongly influenced by underlying rock type, but that once rock type is controlled for, there is a clear positive relationship between uplift and channel steepness. This indicates that uplift is

controlling channel steepness though increased erosion and emphasizes the role of local and regional tectonics on the geomorphologic evolution of a forearc.

The two northernmost basins sampled for cosmogenic ^{10}Be (sites 5 and 6) showed anomalously high apparent erosion rates that exceed all other sites along the Wairarapa and even surpass that of the monsoon-soaked southern Himalaya (Table 1) (Burbank et al., 2012). The low ^{10}Be concentrations with very high uncertainties may not be reflective of rapid erosion over the long term in the following circumstances: (1) cultivation and tilling has removed or mixed significant material within the ^{10}Be accumulation zone (Hewawasam et al., 2003; Schmidt et al, 2016), (2) material below the ^{10}Be accumulation zone is delivered to the channel via gullying (i.e. Reusser and Bierman, 2010; von Blanckenburg et al., 2004), or (3) land use changes trigger a rapid pulse of denudation by abundant shallow landsliding that is not reflective of the long term erosion process or rate (Niemi et al., 2005; Yanites et al., 2009).

Human influence on erosion rates through modern agricultural land use has been documented to occur through a combination of deep tilling and soil loss due to sheet wash after removal of native vegetation (Hewawasam et al., 2003; Schmidt et al, 2016). When the upper layers of soil are mixed via deep tilling (30 - 60 cm), ^{10}Be-poor sediment from below the accumulation zone is carried to the surface. During heavy precipitation events, the loose and newly mixed top layers of soil can be washed away due to the lack of vegetation. When sampled for cosmogenic ^{10}Be, heavily cultivated fluvial basins that practice soil tillage, were found to have 2.5 times greater erosion rates than background levels due to the low ^{10}Be concentration in the sediment artificially inflating the erosion rates (Schmidt et al, 2016). Although a significant portion of the Wairarapa coastline is devoted to agricultural land use through livestock grazing, there is a negligible amount allotted to crop lands where soil is tilled. Thus, land use due to

cultivation is not thought to be a contributing factor to the anomalously high erosion rates along the coastline. Additionally, because livestock are unlikely to be mixing sediment to depths of ~60 cm, and because root structures of the vegetation are generally kept intact, we do not consider animal agriculture to be a strong influence on the calculated erosion rates.

Sites 5 and 6 are entirely underlain by cover sequence bedrock and alluvial sediments from early Miocene and younger (Figure S3). This association contrasts the other seven basins which were fully (sites 2, 3 and 4) or partially (sites 1, 7, 8, and 9) eroded into the denser, lower Cretaceous basement bedrock. These younger, less consolidated, sedimentary deposits are particularly vulnerable to hillslope erosion from gullying and landsliding, especially when exposed to tectonic forcing such as uplift and earthquake shaking. Deeply sourced gully and landslide sediment will have little (if any) ^{10}Be, as sediment would have likely been sourced from below the zone of ^{10}Be production (von Blanckenburg et al., 2004). Mass wasting events of this kind can inundate the mainstem channel with deeply sourced sediment, lowering the concentration of ^{10}Be in the mixed sediment collected at the basin outlet. Previous studies analyzing erosion and sediment dynamics in the Waipaoa River Basin (~130 km north of Cape Kidnappers) determined that gullying had dramatic influence on the basin's overall cosmogenic nuclide signature (Reusser and Bierman, 2010).

The last 180 years have brought significant changes to the New Zealand landscape including European settlement around 1840, when large regions of the Wairarapa coastline were deforested for livestock grazing, predominantly affecting the central and northern basins (sites 5 through 9). The expansive gully complexes seen in the Waipaoa River Basin (north of the Wairarapa coast) were demonstrated to be due to extensive regions of deforestation which created hillslopes prone to gullying and subsequently had a large influence on fluvial aggradation

in the mainstem (Gomez et al., 2003). Similar deforestation, in combination with the weaker underlying lithology in sites 5 and 6, are likely contributing to the gully-style erosion present in these northernmost basins (Figure S4) and the subsequent erroneously high erosion rates.

Erosion Rates and Topographic metrics as indicators of deformation

Previous studies have found strong correlations between channel steepness, uplift rate, and other topographic metrics in tectonically active regions (e.g. Kirby and Whipple, 2001; Duvall et al., 2004; Cyr et al., 2010; Duvall et al., 2019) however, this is consistent with our results only in areas where channels are carved into uniform rock type. There is no strong correlation between channel steepness and uplift rate when evaluating the entire dataset as a whole (Figure 5e), and therefore my analysis demonstrates that channel steepness is not a strong metric with which to identify upper plate deformation (i.e. uplift/erosion rate) in river catchments with heterogeneous bedrock (Figure 5e, f). However, once the dataset is narrowed to the Aorangi Range where the mountains have been actively uplifting for hundreds of thousands years, and the underlying bedrock is consistent, there is a strong correlation between k_{sn} and uplift rate (Figure 6). Furthermore, once the data points from sites 5 and 6 are removed, I observe strong correlations between erosion rate and other metrics such as coupling (Figure 8), highlighting an apparent relationship between the current subduction coupling pattern, erosion, and forearc topography.

Given that the high uplift rates in the Aorangi Range appear to correlate with increased relief and channel steepness values, it is likely that uplift there is controlling erosion in these basins. The high relative uplift rates, erosion rates, and elevation in the Aorangi Range may be a consequence of it lying directly above the locked portion of the megathrust (Figure 1b) and can explain the presence of the oldest basement unit's exposure at the surface. Michel et al. (2022)

suggests that permanent (inelastic) deformation in megathrust subduction environments is typically found where topography is highest. This might indicate that uplift is accumulating over time and inelastic strain is being retained. Alternatively, it is possible that the uplift pattern is more dependent on other localized subduction or upper plate processes. Long-term activity on upper plate faults like the nearby Palliser-Kaiwhata fault (Figure 3a, S1) could be driven by either increased stresses from the underlying locked megathrust or simply higher slip rates on those structures.

Subduction coupling and upper plate faulting

The transition along the Hikurangi margin from large-scale forearc shortening to dextral strike-slip, can heavily impact geomorphology and basin erosion and is an important potential influence on long-term forearc evolution (Kelsey et al., 1995; Lee and Begg, 2002). As regional patterns of deformation are identified, we are able to discern whether upper plate faulting or deeper subduction process (plate coupling, sediment underplating, subduction of buoyant crust, seamount subduction, etc.) are ultimately driving changes in morphology in the overriding forearc (Litchfield et al., 2007). However, unusual faulting patterns and variable uplift rates observed along the Wairarapa coastline (Figure 4c) make it difficult to identify which of these processes are forcing vertical landscape movement. It is also important to consider that any pattern that existed previously, may be overprinted by erosional patterns that are more strongly controlled by underlying rock type.

Numerical models conducted by Litchfield et al. (2007) suggest that sediment underplating (Figure 2d) is the most probable mechanism for higher uplift rates along the inland Axial Ranges, due to the relatively high localized uplift rates (>4 mm/yr), at very short wavelengths that cannot be attributed to upper-plate reverse faults. Conversely, the low

widespread uplift rates along the entire eastern coastline are more extensive and longstanding, indicating that they have been generated by the subduction of an expansive buoyant oceanic plateau (Figure 2f) (Litchfield et al., 2007). The highest erosion rates in our study area (excluding the points near Cape Kidnappers), are found in the Aorangi Range where the uplift rates are highest and appear to correlate well with other topographic metrics. This is the region underlain by the strongest coupling on the megathrust interface which may be triggering more frequent movement on upper plate faults. However, for the rest of the coastline, long term uplift rate does not completely correlate to subduction zone coupling, which would have been expected to steadily decrease moving north towards Cape Turnagain. Instead, there is a pattern of steady fluctuations in the marine terrace uplift rates at a wavelength of approximately 100 kilometers (Figure 4c). In general, a ~100 km wavelength structure is not short enough to be attributed to underplated sediments as is seen in the Axial Ranges, but is instead more similar to the wavelength of local offshore upper plate reverse faults (e.g. Palliser-Kaiwhata fault) (Figure S1) (Litchfield et al., 2007, Litchfield et al., 2021).

Upper plate faults that splay to the subduction interface play an important role in accommodating margin-normal shortening along the HSZ, and the Wairarapa coastline hosts several faults with historic evidence of localized coastal deformation (i.e marine terraces). Because uplift rate is not uniform across the Wairarapa coastline (as would be expected if uplift was purely influenced by subduction earthquakes), and the wavelength is too long to be attributed to more localized subduction features like sediment underplating, it is most reasonably attributed to single or multi-fault rupture parallel to the subduction margin. However, uplift rates still appear to peak in the regions overlying strong subduction coupling (Aorangi Range) despite lower, variable uplift rates along the rest of the coastline. This may indicate that although slip on

upper plate faults is occurring at sites located along the entire coastline, strong subduction coupling is initiating faster and more frequent slip (and uplift) on upper plate faults in this zone in particular. This provides further evidence that some component of convergent motion is being absorbed in the forearc as megathrust earthquakes are triggering slip on upper plate faults.

6. Conclusion

By establishing links between basin geomorphology, which have developed and evolved over millennia and throughout multiple earthquake cycles, and underlying subduction zone processes, we are better able to predict how future megathrust earthquakes may influence landscape evolution over longer time periods. For this study, I used digital and erosion analyses to investigate the mechanisms that influence topographic patterns in a dynamic and tectonically active landscape. Several important conclusions are indicated from this analysis:

1. Underlying rock type in fluvial basins exerts a fundamental control on channel steepness. Our dataset indicates a strong correlation between uplift and channel steepness where basins are underlain by competent, homogeneous lithology. Conversely, channels underlain by weaker or mixed lithology show weak relationships between channel steepness, erosion, and other topographic metrics suggesting that their tectonic signature is being muddled or erased due to variations in underlying lithology.
2. Once controlled for underlying rock type, there is a strong correlation between channel steepness and coastal uplift rate (as measured from marine terraces), indicating that uplift is likely a key driver of geomorphic evolution in the forearc basins.
3. In the region where we see the deepest exhumation and highest topography (e.g. Aorangi Range), erosion and coastal uplift generally agree over millennia, potentially indicating that the zone of coupling is stable over geological time and ultimately driving

the higher rates of uplift. The control on uplift rate seen in the Aorangi Range could reflect (1) long-term activity on upper plate faults (i.e. Palliser-Kaiwhata fault) driven by either increased stresses from the underlying locked megathrust or simply higher slip rates on those structures, or (2) a direct result of its location directly above the locked portion of the megathrust.

Although the HSZ provides a unique location to study basin morphology in response to variations in subduction zone coupling, my results emphasize the importance of controlling for rock type when examining uplift, erosion, and other deformational patterns across a forearc. After careful consideration is given to underlying geology, a relationship between subduction coupling, uplift, and erosion in the Aorangi Range suggests long-term stability of the locked zone and demonstrates that coupling is a key driver of long-term forearc erosion and topographic development along the Hikurangi subduction margin.

Supplemental Figures and Tables

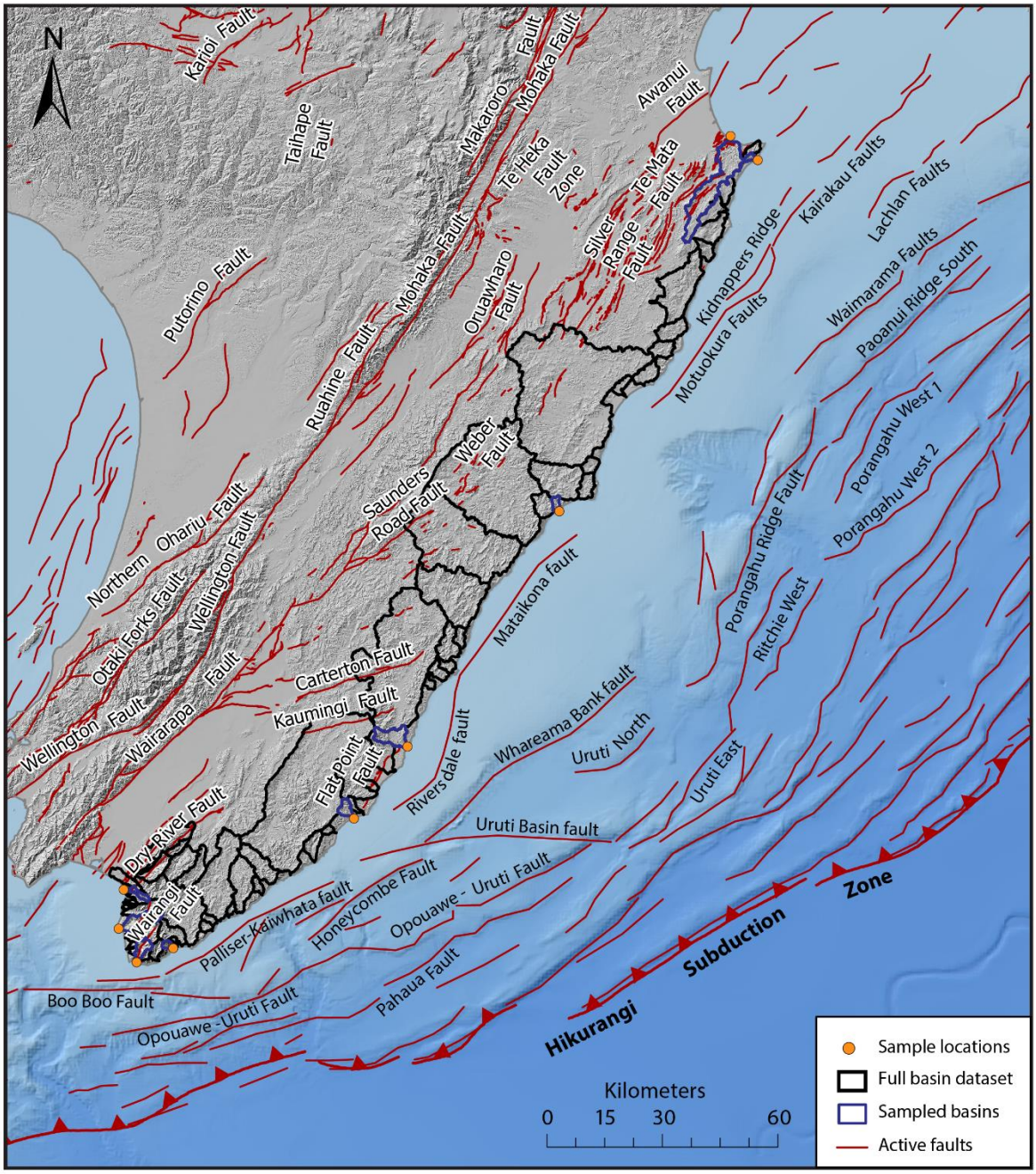

Figure S1: Active tectonic map of the Hikurangi Subduction Margin. Offshore fault dataset compiled from Barnes and Audru (1999), Barnes et al. (2002, 2010), Nodder et al. (2007), Berryman et al. (2011), Litchfield et al. (2014), Mountjoy et al. (2009), Pondard and Barnes (2010), Mountjoy and Barnes (2011), Paquet et al. (2009). Onshore active fault dataset sourced from the New Zealand Active Faults Database (Langridge et al., 2016). Bathymetry dataset sourced from the National Institute of Water and Atmospheric Research (NIWA) (Mitchell et al., 2012).

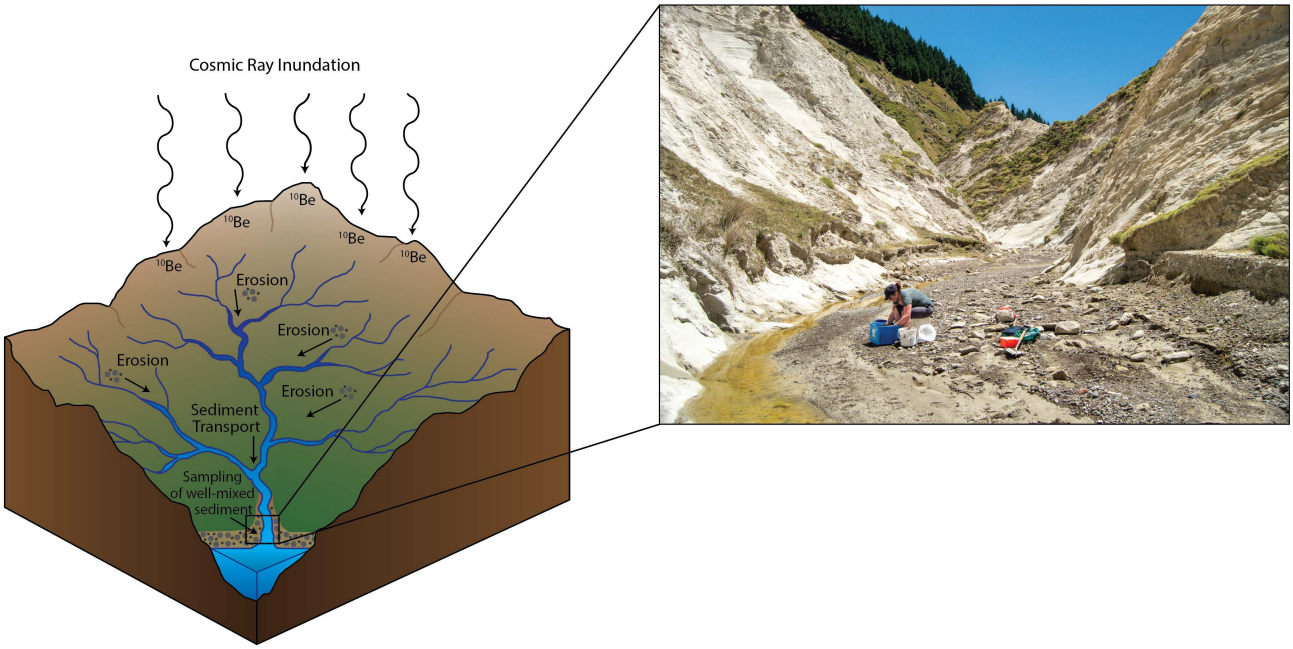

Figure S2: Graphical diagram (left) illustrating the accumulation of cosmogenic ^{10}Be and the subsequent mixing of eroded sediment in a typical basin. This process allows us to obtain a basin-averaged measurement of erosion rate by sampling at the basin outlet. Photograph showing sample site 6 (basin 59), one of the nine basin outlets where sediment was sampled for ^{10}Be.

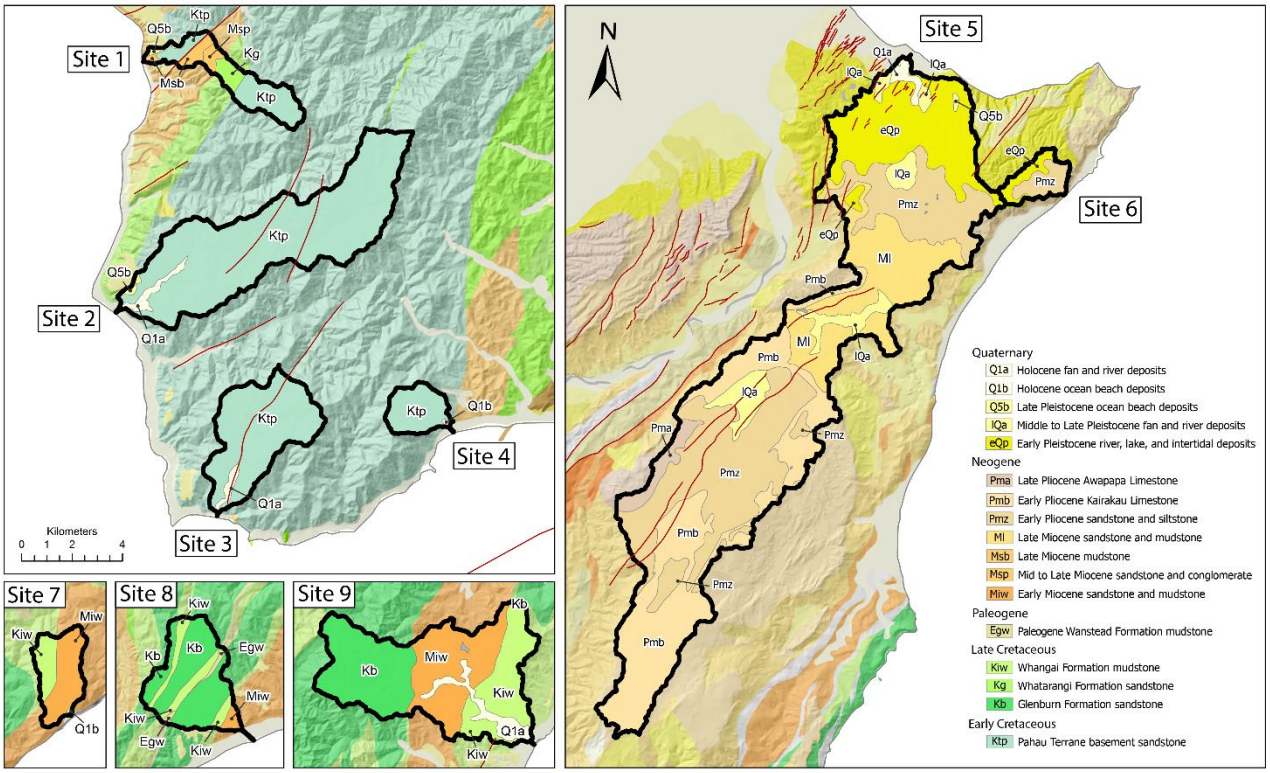

Figure S3: Geologic map of basins sampled for ^{10}Be cosmogenic erosion analysis. Geologic units and bedrock faults are from Begg and Johnston (2000) and Lee and Begg (2002).

Figure S4: Gullying within the site 6 river basin. Satellite imagery from Google Earth, March 2018.

Table S1: Basin-averaged metrics for full dataset

*Basin Name**	*Basin ID*[†]	*Uplift Rate*[¶] *(mm/yr)*	*Mean Precipitation*[§] *(mm/yr)*	*Minimum Precipitation*[§] *(mm/yr)*	*Maximum Precipitation*[§] *(mm/yr)*	*Coupling*[#] *(outlet)*	*Drainage area*** *(km²)*	*Mean k_{sn}***	*Mean gradient***	*Mean relief*** *(2.5km radius) (m)*	*Mean slope*[††] *(degree)*
Whangaimoana Stream	1	0.410 ± 0.5	1492	1076	2055	1 ± 0.102	19.4	40.2 ± 4.4	0.23 ± 0.0007	313 ± 0.42	16.9 ± 13.7
Hurupi Stream	2	0.510 ± 0.5	1573	1076	2055	1 ± 0.139	7.2	95.1 ± 7.1	0.48 ± 0.0011	527 ± 0.39	32.9 ± 11.3
Putangirua Stream	3	0.550 ± 0.5	1578	1076	2055	1 ± 0.139	6.8	107.0 ± 22.6	0.45 ± 0.0011	538 ± 0.37	31.3 ± 11.4
Te Kapi Stream	4	0.58 ± 0.5	1574	1076	2055	1 ± 0.081	2.5	89.5 ± 8.9	0.44 ± 0.0018	485 ± 0.17	30.5 ± 11.1
Whatarangi Stream	5	0.62 ± 0.5	1565	1113	2011	1 ± 0.081	1.5	69.8 ± 0	0.41 ± 0.0023	473 ± 0.29	28.8 ± 11.7
Wakapirihika Stream	6	0.69 ± 0.5	1562	1113	2011	1 ± 0.081	2.1	66.1 ± 0	0.30 ± 0.0019	385 ± 0.02	22.0 ± 12.4
Makotukutuku Stream	7	0.810 ± 0.5	1542	1076	2055	1 ± 0.049	21.5	93.1 ± 6.5	0.52 ± 0.0007	572 ± 0.26	35.1 ± 11.2
Pararaki Stream	8	1.130 ± 0.5	1488	1076	2055	1 ± 0.013	33.8	84.5 ± 8.0	0.51 ± 0.0005	595 ± 0.18	34.4 ± 11.6
Otakaha Stream	9	1.310 ± 0.5	1455	1113	2011	1 ± 0.002	34.5	97.5 ± 12.5	0.54 ± 0.0005	638 ± 0.26	35.8 ± 11.7
Waiahero Stream	10	1.49 ± 0.5	1249	1180	1270	1 ± 0.005	2.5	115.0 ± 0	0.50 ± 0.0018	602 ± 0.13	34.1 ± 10.4
Blueslip Creek	11	1.58 ± 0.5	1253	1187	1270	1 ± 0.005	2.5	88.5 ± 0	0.52 ± 0.0019	605 ± 0.00	35.2 ± 11.1
Mangatoetoe Stream	12	1.940 ± 0.5	1362	1180	1587	1 ± 0.008	14.4	97.3 ± 13.8	0.54 ± 0.0008	734 ± 0.29	35.9 ± 11.2
Little Mangatoetoe Stream	13	1.94 ± 0.5	1270	1187	1270	1 ± 0.008	4.8	174.0 ± 61.1	0.53 ± 0.0014	752 ± 0.53	35.5 ± 11.1
Waitetuna Stream	14	2.380 ± 0.5	1428	1270	1587	1 ± 0.018	12.4	172.9 ± 35.4	0.60 ± 0.0009	786 ± 0.23	38.8 ± 10.5
Waiarakeke Stream	15	2.66 ± 0.5	1434	1333	1587	1 ± 0.017	4.0	150.1 ± 30.5	0.58 ± 0.0017	886 ± 0.04	37.6 ± 11.4
White Rock	16	2.71 ± 0.5	1406	1333	1587	1 ± 0.017	2.6	44.7 ± 0	0.35 ± 0.0017	656 ± 0.42	25.4 ± 11.4
Whawanui River	17	2.790 ± 0.5	1427	1113	2011	1 ± 0.017	27.1	72.3 ± 12.4	0.46 ± 0.0007	623 ± 0.35	30.9 ± 14.1
Opouawe River	18	2.850 ± 0.5	1277	1076	2055	1 ± 0.017	105.1	56.0 ± 4.2	0.37 ± 0.0003	495 ± 0.26	26.1 ± 13.1
Pukemuri Stream	19	3.030 ± 0.5	1303	1113	1443	1 ± 0.014	7.5	64.7 ± 15.0	0.30 ± 0.0009	390 ± 0.11	22.4 ± 10.2
Awheaiti Stream	20	3.050 ± 0.5	1193	1113	1355	1 ± 0.017	7.5	59.0 ± 11.9	0.30 ± 0.0008	399 ± 0.12	22.2 ± 9.8
Awhea River	21	3.050 ± 0.5	1176	1076	1762	1 ± 0.017	151.5	31.0 ± 2.4	0.29 ± 0.0002	317 ± 0.08	21.4 ± 10.7
Hungaroa Stream	22	3.040 ± 0.5	1113	1076	1264	1 ± 0.01	5.3	44.4 ± 3.9	0.33 ± 0.0010	308 ± 0.08	24.1 ± 9.9
Oterei River	23	3.000 ± 0.5	1168	1076	1279	0.991 ± 0.034	65.4	40.8 ± 5.3	0.33 ± 0.0003	342 ± 0.14	23.7 ± 11.5
Okoropunga Stream	24	2.800 ± 0.5	1165	1076	1235	0.972 ± 0.056	8.8	79.8 ± 8.5	0.45 ± 0.0011	481 ± 0.15	31.0 ± 11.8
Rerewhakaaitu River	25	2.640 ± 0.5	1174	1163	1279	0.952 ± 0.081	46.9	44.0 ± 5.1	0.34 ± 0.0004	350 ± 0.16	24.7 ± 11.5
Rahaoa River	26	2.400 ± 0.5	1162	920	1385	0.954 ± 0.084	647.3	43.4 ± 2.4	0.27 ± 0.0001	340 ± 0.06	19.6 ± 12.3
Waihingaia Stream	27	2.020 ± 0.5	1176	1160	1177	0.917 ± 0.139	21.7	101.2 ± 15.0	0.36 ± 0.0006	512 ± 0.26	25.9 ± 10.7
Waikekino Stream	28	1.440 ± 0.5	1177	1177	1177	0.895 ± 0.167	5.7	119.1 ± 24.3	0.30 ± 0.0010	500 ± 0.19	22.3 ± 10.1
Arawhata Stream	29	1.140 ± 0.5	1170	1099	1301	0.875 ± 0.196	11.8	64.7 ± 5.4	0.36 ± 0.0007	429 ± 0.20	26.4 ± 9.8
Te Una Una Stream	30	1.040 ± 0.5	1128	1099	1301	0.875 ± 0.196	6.8	54.4 ± 7.4	0.32 ± 0.0009	342 ± 0.30	23.1 ± 10.7
Kaiwhata River	31	0.750 ± 0.5	1122	1070	1385	0.85 ± 0.227	101.5	49.8 ± 4.8	0.33 ± 0.0003	368 ± 0.08	23.9 ± 11.7
Waiohuru Stream	32	0.710 ± 0.5	1090	1070	1154	0.83 ± 0.257	9.4	34.4 ± 5.8	0.19 ± 0.0008	298 ± 0.51	14.4 ± 11.6
Patanui Stream	33	0.600 ± 0.5	1117	1070	1204	0.823 ± 0.26	43.2	41.7 ± 6.2	0.26 ± 0.0005	336 ± 0.28	19.2 ± 13.6
Motuwaireka Stream	34	0.430 ± 0.5	1113	1108	1204	0.808 ± 0.282	31.2	51.0 ± 8.0	0.29 ± 0.0005	381 ± 0.32	21.3 ± 12.2
Whareama River	35	0.430 ± 0.5	1189	1028	1364	0.796 ± 0.28	532.3	35.2 ± 1.8	0.27 ± 0.0001	321 ± 0.04	19.8 ± 11.1
Otahome Stream	36	0.540 ± 0.5	1067	1066	1068	0.796 ± 0.291	6.9	48.1 ± 16.7	0.28 ± 0.0008	351 ± 0.31	21.2 ± 9.5
Ngakauau Stream	37	0.610 ± 0.5	1071	1067	1102	0.791 ± 0.295	15.8	53.5 ± 13.5	0.32 ± 0.0006	361 ± 0.21	23.5 ± 10.7

Castlepoint Stream	38	0.770 ± 0.5	1073	1067	1075	0.797 ± 0.294	10.7	36.8 ± 9.9	0.30 ± 0.0007	313 ± 0.27	22.0 ± 10.2
Whakataki River	39	0.860 ± 0.5	1144	1075	1292	0.791 ± 0.298	38.3	67.1 ± 23.4	0.35 ± 0.0004	336 ± 0.10	25.2 ± 11.4
Okau Stream	40	0.950 ± 0.5	1103	1103	1292	0.791 ± 0.298	12.6	54.1 ± 12.4	0.38 ± 0.0007	413 ± 0.17	27.3 ± 10.2
Mataikona River	41	1.190 ± 0.5	1270	1103	1343	0.78 ± 0.301	190.2	54.2 ± 3.6	0.32 ± 0.0002	380 ± 0.07	23.5 ± 10.9
Owahanga River	42	1.600 ± 0.5	1168	1116	1502	0.755 ± 0.304	400.4	42.5 ± 2.6	0.27 ± 0.0001	326 ± 0.07	19.7 ± 11.2
Akitio River	43	1.770 ± 0.5	1176	1116	1502	0.697 ± 0.310	589.3	44.8 ± 3.5	0.26 ± 0.0001	307 ± 0.06	19.2 ± 10.8
Waimata River	44	1.790 ± 0.5	1155	1149	1168	0.609 ± 0.298	27.3	56.6 ± 9.2	0.32 ± 0.0004	368 ± 0.09	23.3 ± 9.5
Papuka Stream	45	1.800 ± 0.5	1153	1153	1168	0.62 ± 0.297	5.9	46.4 ± 7.1	0.33 ± 0.0009	279 ± 0.04	24.1 ± 9.5
Wainui River	46	1.700 ± 0.5	1183	1153	1213	0.629 ± 0.298	100.8	43.0 ± 3.5	0.27 ± 0.0002	293 ± 0.06	20.4 ± 10.0
Tautane Stream	47	1.710 ± 0.5	1155	1154	1177	0.629 ± 0.298	21.9	19.7 ± 3.2	0.28 ± 0.0005	246 ± 0.07	21.0 ± 10.7
Whangaehu River	48	1.470 ± 0.5	1185	1177	1213	0.629 ± 0.301	14.4	33.1 ± 7.7	0.21 ± 0.0004	280 ± 0.08	16.4 ± 7.9
Porangahau River	49	1.250 ± 0.5	1062	837	1213	0.509 ± 0.252	819.6	34.8 ± 1.8	0.19 ± 0.0001	255 ± 0.05	14.8 ± 10.7
Unnamed (Glenellen)	50	1.190 ± 0.5	1065	1017	1066	0.434 ± 0.218	12.4	11.2 ± 3.5	0.16 ± 0.0005	164 ± 0.11	12.6 ± 8.7
Waikaraka Stream	51	1.170 ± 0.5	1059	1057	1089	0.367 ± 0.185	24.6	25.1 ± 5.9	0.19 ± 0.0004	199 ± 0.07	14.3 ± 9.4
Ouepoto Stream	52	1.260 ± 0.5	1080	1057	1119	0.234 ± 0.117	22.8	37.1 ± 7.9	0.24 ± 0.0004	248 ± 0.11	18.0 ± 10.0
Pourerere Stream	53	1.400 ± 0.5	1095	1084	1126	0.234 ± 0.117	31.9	37.9 ± 4.9	0.23 ± 0.0004	311 ± 0.27	17.2 ± 9.7
Mangakuri River	54	1.910 ± 0.5	1295	1090	1466	0.032 ± 0.017	116.9	48.6 ± 4.9	0.22 ± 0.0002	348 ± 0.10	16.4 ± 10.3
Te Apiti Stream	55	1.980 ± 0.5	1451	1450	1466	0 ± 0	16.8	115.9 ± 23.9	0.27 ± 0.0006	506 ± 0.24	19.9 ± 10.3
Puhokio Stream	56	2.040 ± 0.5	1209	1170	1537	0 ± 0	40.1	73.5 ± 11.0	0.20 ± 0.0003	409 ± 0.21	15.1 ± 9.5
Waingongoro Stream	57	2.020 ± 0.5	1212	1170	1532	0 ± 0	24.3	83.9 ± 25.6	0.14 ± 0.0004	305 ± 0.18	11.2 ± 8.8
Waipuka Stream	58	1.850 ± 0.5	1127	1015	1170	0 ± 0	18.9	36.9 ± 5.9	0.20 ± 0.0002	307 ± 0.13	16.0 ± 9.6
Unnamed (Rangaiika)	59	1.5 ± 0.5	791	769	812	0 ± 0	3.7	62.2 ± 25.3	0.37 ± 0.0015	270 ± 0.00	26.2 ± 11.8
Unnamed (Cape Kidnappers)	60	1.2 ± 0.5	791	769	812	0 ± 0	9.2	37.5 ± 4.0	0.28 ± 0.0009	235 ± 0.10	20.6 ± 12.0
Maraetotara River	61	1.33 ± 0.5	1176	769	1537	0 ± 0	117.1	51.1 ± 6.3	0.20 ± 0.0001	269 ± 0.06	15.4 ± 10.6
Turanganui River	62	*Inland*	1425	1076	2055	1 ± 0.147	44.1	103.8 ± 8.0	0.52 ± 0.0004	693 ± 0.18	35.2 ± 10.8
Tauanui River	63	*Inland*	1355	1076	2055	1 ± 0.147	29.2	111.6 ± 14.1	0.53 ± 0.0003	704 ± 0.14	34.9 ± 11.3
Whangaehu Stream	64	*Inland*	1423	1163	1860	1 ± 0.174	3.8	65.3 ± 3.5	0.46 ± 0.0007	492 ± 0.36	31.5 ± 10.4
Waihora Stream	65	*Inland*	1251	1077	1482	1 ± 0.12	16.0	97.4 ± 9.0	0.43 ± 0.0008	667 ± 0.35	29.8 ± 12.4
Granny's Creek	66	*Inland*	1183	1077	1482	1 ± 0.139	4.9	79.8 ± 10.4	0.36 ± 0.0006	573 ± 0.29	26.3 ± 10.9
Dry River	67	*Inland*	1193	869	1482	0.958 ± 0.18	30.4	68.9 ± 13.3	0.31 ± 0.0003	384 ± 0.21	22.5 ± 13.5
Blue Rock Stream	68	*Inland*	1236	1098	1482	0.987 ± 0.22	11.8	78.7 ± 6.2	0.40 ± 0.0009	495 ± 0.41	28.2 ± 12.4
Ruakokoputuna River	69	*Inland*	1281	1076	2055	0.988 ± 0.215	45.9	90.4 ± 7.1	0.40 ± 0.0004	555 ± 0.24	28.1 ± 11.4
Makara River	70	*Inland*	1246	1076	2055	0.988 ± 0.215	38.4	82.6 ± 14.6	0.34 ± 0.0004	435 ± 0.23	24.8 ± 11.4

Note: Basins highlighted in blue were sampled for ^{10}Be and are the only sites with erosion rate measurements (Table 1). Basins highlighted in gray do not drain to the coastline and do not have associated uplift measurements.
*River names are based on the cartographic text shown on NZ Topo50 maps as of December 2021. Source: LINZ database (https://data.linz.govt.nz).
† Basins are numbered sequentially from south to north.
¶ Uplift measurements calculated using Beavan and Litchfield (2012) data compilation and N. Litchfield (personal communication, March 2020). Quoted uncertainty of ± 0.5 is a midway value between the full dataset's standard deviation (0.73) and the average uplift uncertainty (0.34).
§ Values based on average annual precipitation from 1972-2013. Annual rainfall is estimated from daily rainfall data collected by the National Institute for Water and Atmospheric Research (NIWA), Virtual Climate Station Network.
# Coupling values calculated using data published in Wallace et al. (2012b).
** Topographic metrics (drainage area, mean k_{sn}, mean gradient, mean relief) were calculated using the Topographic Analysis Kit (Forte and Whipple, 2019) in conjunction with Topotoolbox (Schwanghart and Kuhn, 2010).
†† Slope is calculated as a statistical output through the Esri ArcPro 'Slope' tool using a 3x3 cell moving window which is then averaged across the basin.

7. References

Ahnert, F., 1970, Functional relationships between denudation, relief, and uplift in large, mid-latitude drainage basins: American Journal of Science, v. 268, p. 243–263, doi:10.2475/ajs.268.3.243.

Allen, G.H., Barnes, J.B., Pavelsky, T.M., and Kirby, E., 2013, Lithologic and tectonic controls on bedrock channel form at the northwest Himalayan front: Journal of Geophysical Research: Earth Surface, v. 118, p. 1806–1825, doi:10.1002/jgrf.20113.

Balco, G., Finnegan, N., Gendaszek, A., Stone, J.O.H., and Thompson, N., 2013, Erosional response to northward-propagating crustal thickening in the coastal ranges of the U.S. Pacific Northwest: American Journal of Science, v. 313, p. 790–806, doi:10.2475/11.2013.01.

Ballance, P.F., 1976, Evolution of the Upper Cenozoic Magmatic Arc and plate boundary in northern New Zealand: Earth and Planetary Science Letters, v. 28, p. 356–370, doi:10.1016/0012-821X(76)90197-7.

Barnes, P.M., and Audru, J., 1999, Quaternary faulting in the offshore Flaxbourne and Wairarapa Basins, southern Cook Strait, New Zealand: New Zealand Journal of Geology and Geophysics, v. 42, p. 349–367, doi:10.1080/00288306.1999.9514851.

Barnes, P.M., Lamarche, G., Bialas, J., Henrys, S., Pecher, I., Netzeband, G.L., Greinert, J., Mountjoy, J.J., Pedley, K., and Crutchley, G., 2010, Tectonic and geological framework for gas hydrates and cold seeps on the Hikurangi subduction margin, New Zealand: Marine Geology, v. 272, p. 26–48, doi:10.1016/j.margeo.2009.03.012.

Barnes, P.M., Nicol, A., and Harrison, T., 2002, Late Cenozoic evolution and earthquake potential of an active listric thrust complex above the Hikurangi subduction zone, New Zealand: Geological Society of America Bulletin, v. 114, p. 1379–1405, doi:10.1130/0016-7606

Beanland, S., and Haines, J., 1998, The kinematics of active deformation in the North Island, New Zealand, determined from geological strain rates: New Zealand Journal of Geology and Geophysics, v. 41, p. 311–323, doi:10.1080/00288306.1998.9514813.

Beavan, J., and Haines, J., 2001, Contemporary horizontal velocity and strain rate fields of the Pacific-Australian plate boundary zone through New Zealand: Journal of Geophysical Research: Solid Earth, v. 106, p. 741–770, doi:10.1029/2000JB900302.

Beavan, R.J., and Litchfield, N.J., 2012, Vertical land movement around the New Zealand coastline: implications for sea-level rise: Lower Hutt, N.Z., GNS Science.

Begg, J., and Johnston, M.R., 2000, Geology of the Wellington Area: Institute of Geological and Nuclear Sciences 1:250,000 Geological Map, v. 10, p. 1–70.

Berryman, K., Ota, Y., Miyauchi, T., Hull, A., Clark, K., Ishibashi, K., Iso, N., and Litchfield, N., 2011, Holocene Paleoseismic History of Upper-Plate Faults in the Southern Hikurangi Subduction Margin, New Zealand, Deduced from Marine Terrace Records Holocene Paleoseismic History of Upper-Plate Faults in the Southern Hikurangi Subduction Margin, New Zealand: Bulletin of the Seismological Society of America, v. 101, p. 2064–2087, doi:10.1785/0120100282.

Bierman, P., and Steig, E.J., 1996, Estimating Rates of Denudation Using Cosmogenic Isotope Abundances in Sediment: Earth Surface Processes and Landforms, v. 21, p. 125–139, doi:10.1002/(SICI)1096-9837(199602)

Brown, E.T., Stallard, R.F., Larsen, M.C., Raisbeck, G.M., and Yiou, F., 1995, Denudation rates determined from the accumulation of in situ-produced ^{10}Be in the luquillo experimental forest, Puerto Rico: Earth and Planetary Science Letters, v. 129, p. 193–202, doi:10.1016/0012-821X(94)00249-X.

Burbank, D.W., Bookhagen, B., Gabet, E.J., and Putkonen, J., 2012, Modern climate and erosion in the Himalaya: Comptes Rendus Geoscience, v. 344, p. 610–626, doi:10.1016/j.crte.2012.10.010.

Charreau, J., Blard, P.-H., Zumaque, J., Martin, L.C.P., Delobel, T., and Szafran, L., 2019, Basinga: A cell-by-cell GIS toolbox for computing basin average scaling factors, cosmogenic production rates and denudation rates: Earth Surface Processes and Landforms, v. 44, p. 2349–2365, doi:10.1002/esp.4649.

Clark, K., Howarth, J., Litchfield, N., Cochran, U., Turnbull, J., Dowling, L., Howell, A., Berryman, K., and Wolfe, F., 2019, Geological evidence for past large earthquakes and tsunamis along the Hikurangi subduction margin, New Zealand: Marine Geology, v. 412, p. 139–172, doi:10.1016/j.margeo.2019.03.004.

Clift, P., 2004, Controls on tectonic accretion versus erosion in subduction zones: Implications for the origin and recycling of the continental crust: Reviews of Geophysics, v. 42, p. RG2001, doi:10.1029/2003RG000127.

Cloos, M., 1993, Lithospheric buoyancy and collisional orogenesis: Subduction of oceanic plateaus, continental margins, island arcs, spreading ridges, and seamounts: GSA Bulletin, v. 105, p. 715–737, doi:10.1130/0016-7606

Columbus, J.; Sirguey, P. & Tenzer, R. (2011), “NZSoSDEM v1.0”, A free, fully assessed 15-m DEM for New Zealand, Survey Quarterly 66, 16-19.

Cyr, A.J., Granger, D.E., Olivetti, V., and Molin, P., 2010, Quantifying rock uplift rates using channel steepness and cosmogenic nuclide–determined erosion rates: Examples from northern and southern Italy: Lithosphere, v. 2, p. 188–198, doi:10.1130/L96.1.

Darby, D., and Beavan, J., 2001, Evidence from GPS measurements for contemporary interplate coupling on the southern Hikurangi subduction thrust and for partitioning of strain in the

upper plate: Journal of Geophysical Research: Solid Earth, v. 106, p. 30881–30891, doi:10.1029/2000JB000023.

Davy, B.W., 1992, The Influence of Subducting Plate Buoyancy on Subduction of the Hikurangi-Chatham Plateau beneath the North Island, New Zealand, in Advances in the Geology and Geophysics of the Continental Margin, v. 53, p. 75–91. doi:10.1306/M53552C6

Delano, J.E., Lynch, E.M., Amos, C.B., Loveless, J.P., Rittenour, T.M., and Sherrod, B.L., 2017, Influence of the megathrust earthquake cycle on upper-plate deformation in the Cascadia forearc of Washington State, USA: Geology, v. 45, p. 1051–1054, doi:10.1130/g39070.1.

DiBiase, R.A., Whipple, K.X., Heimsath, A.M., and Ouimet, W.B., 2010, Landscape form and millennial erosion rates in the San Gabriel Mountains, CA: Earth and Planetary Science Letters, v. 289, p. 134–144, doi:10.1016/j.epsl.2009.10.036.

Dominguez, S., Lallemand, S.E., Malavieille, J., and von Huene, R., 1998, Upper plate deformation associated with seamount subduction: Tectonophysics, v. 293, p. 207–224, doi:10.1016/S0040-1951(98)00086-9.

Duckworth, W.C., Amos, C.B., Schermer, E.R., Loveless, J.P., and Rittenour, T.M., 2021, Slip and Strain Accumulation Along the Sadie Creek Fault, Olympic Peninsula, Washington: Journal of Geophysical Research: Solid Earth, v. 126, p. 2020JB020276, doi:10.1029/2020JB020276.

Dunai, T., 2010, Cosmogenic nuclides: principles, concepts and applications in the earth surface sciences. Cambridge: Cambridge University Press. doi:10.1017/CBO9780511804519

Duvall, A., Kirby, E., Burbank, D., 2004, Tectonic and lithologic controls on bedrock channel profiles and processes in coastal California: Journal of Geophysical Research, v. 109, p. F03002, doi:10.1029/2003JF000086.

Duvall, A., Harbert, S., Upton, P., Tucker, G., Flowers, R., and Collett, C., 2019, River patterns reveal landscape evolution at the edge of subduction, Marlborough Fault System, New Zealand: Earth Surface Dynamics Discussions, p. 1–28, doi:10.5194/esurf-2019-41.

Esri Inc. (2021). ArcGIS Pro (Version 2.8.3). Esri Inc. https://www.esri.com/en-us/arcgis/products/arcgis-pro/overview.

Esri, "TopoBathy" [basemap], Scale Not Given, "TopoBathy Elevation Tinted Hillshade", 2014, https://elevation.arcgis.com/arcgis/rest/services/WorldElevation/TopoBathy/ImageServer [Accessed: February 21, 2022].

Fisher, D.M., Gardner, T.W., Marshall, J.S., Sak, P.B., and Protti, M., 1998, Effect of subducting sea-floor roughness on fore-arc kinematics, Pacific coast, Costa Rica: Geology, v. 26, p. 467–470, doi:10.1130/0091-7613

Forte, A.M., and Whipple, K.X., 2019, Short communication: The Topographic Analysis Kit (TAK) for TopoToolbox: Earth Surface Dynamics, v. 7, p. 87–95, doi:https://doi.org/10.5194/esurf-7-87-2019.

Granger, D.E., Kirchner, J.W., and Finkel, R., 1996, Spatially Averaged Long-Term Erosion Rates Measured from in Situ-Produced Cosmogenic Nuclides in Alluvial Sediment: The Journal of Geology, v. 104, p. 249–257.

Gomez, B., Banbury, K., Marden, M., Trustrum, N.A., Peacock, D.H., and Hoskin, P.J., 2003, Gully erosion and sediment production: Te Weraroa Stream, New Zealand: Gully erosion, sediment production, and storage: Water Resources Research, v. 39, doi:10.1029/2002WR001342.

Google Earth Pro v. 7.3.4.8248, (March 26, 2018), Ocean Beach, New Zealand, 39°40'46.79"S 177° 3'51.46"E, Eye altitude: 2,550 feet, http://www.earth.google.com, [Accessed: February 25, 2022].

Gosse, J., and Phillips, F., 2001, Terrestrial in situ cosmogenic nuclides: Theory and application: Quaternary Science Reviews, v. 20, p. 1475–1560, doi:10.1016/S0277-3791(00)00171-2.

Hewawasam, T., von Blanckenburg, F., Schaller, M., and Kubik, P., 2003, Increase of human over natural erosion rates in tropical highlands constrained by cosmogenic nuclides: Geology, v. 31, p. 597–600, doi:10.1130/0091-7613(2003)031<0597:IOHONE>2.0.CO;2

Kelsey, H.M., Cashman, S.M., Beanland, S., and Berryman, K.R., 1995, Structural evolution along the inner forearc of the obliquely convergent Hikurangi margin, New Zealand: Tectonics, v. 14, p. 1–18, doi:10.1029/94TC01506.

Kirby, E., and Whipple, K., 2001, Quantifying differential rock-uplift rates via stream profile analysis: Geology, v. 29, p. 415–418, doi:10.1130/0091-7613

Kohl, C.P., and Nishiizumi, K., 1992, Chemical isolation of quartz for measurement of in-situ -produced cosmogenic nuclides: Geochimica et Cosmochimica Acta, v. 56, p. 3583–3587, doi:10.1016/0016-7037(92)90401-4.

Lal, D., 1988, In Situ-Produced Cosmogenic Isotopes in Terrestrial Rocks: Annual Review of Earth and Planetary Sciences, v. 16, p. 355–388, doi:10.1146/annurev.ea.16.050188.002035.

Lal, D., 1991, Cosmic ray labeling of erosion surfaces: in situ nuclide production rates and erosion models. Earth and Planetary Science Letters, v. 104, p. 424-439, doi: 10.1016/0012-821X(91)90220-C.

Langridge, R. et al., 2016, The New Zealand Active Faults Database: New Zealand Journal of Geology and Geophysics, v. 59, p. 86–96, doi:10.1080/00288306.2015.1112818.

Lee, J., and Begg, J., 2002, Geology of the Wairarapa area: v. 11. Institute of Geological and Nuclear Sciences 1:250,000 Geological Map, 0-478-09750-6.

Lee, J.M.; Townsend, D., Bland, K., Kamp, P.J.J. (compilers) 2011: Geology of the Hawke's Bay area: scale 1:250,000. Lower Hutt: Institute of Geological & Nuclear Sciences Limited. Institute of Geological & Nuclear Sciences 1:250,000 geological map 8. 86 p. + 1 folded map.

Lindsey, E.O., Mallick, R., Hubbard, J.A., Bradley, K.E., Almeida, R.V., Moore, J.D.P., Bürgmann, R., and Hill, E.M., 2021, Slip rate deficit and earthquake potential on shallow megathrusts: Nature Geoscience, v. 14, p. 321–326, doi:10.1038/s41561-021-00736-x.

Litchfield, N.J., and Berryman, K.R., 2005, Correlation of fluvial terraces within the Hikurangi Margin, New Zealand: implications for climate and baselevel controls: Geomorphology, v. 68, p. 291–313, doi:10.1016/j.geomorph.2004.12.001.

Litchfield, N.J., Van Dissen, R.J., Sutherland, R., Barnes, P.M., Cox, S.C., Norris, R., Beavan, R.J., Langridge, R.M. Villamor, P., Berryman, K.R., Stirling, M.W., Nicol, A., Nodder, S.; Lamarche, G., Barrell, D.J.A., Pettinga, J.R., Little, T., Pondard, N., Mountjoy, J.J., Clark, K.J. 2014, A model of active faulting in New Zealand. New Zealand Journal of Geology and Geophysics, 57(1): 32-56; doi: 10.1080/00288306.2013.854256

Litchfield, N.J., and Clark, K.J., 2015, Fluvial terrace formation in the lower Awhea and Pahaoa River valleys, New Zealand: implications for tectonic and sea-level controls: Geomorphology, v. 231, p. 212–228, doi:10.1016/j.geomorph.2014.12.009.

Litchfield, N., Ellis, S., Berryman, K., and Nicol, A., 2007, Insights into subduction-related uplift along the Hikurangi Margin, New Zealand, using numerical modeling: Journal of Geophysical Research, v. 112, p. F02021, doi:10.1029/2006JF000535.

Litchfield, N.J., Howell, A., Clark, K.J., Coffey, G.L., 2021, It's Our Fault Hikurangi Subduction Zone hazard: south Palliser Bay Holocene marine terraces. Lower Hutt, N.Z.: GNS Science. GNS Science report 2021/28. 47 p.; doi: 10.21420/8VDN-AE32

Mazzotti, S., Le Pichon, X., Henry, P., and Miyazaki, S.-I., 2000, Full interseismic locking of the Nankai and Japan-west Kurile subduction zones: An analysis of uniform elastic strain accumulation in Japan constrained by permanent GPS: Journal of Geophysical Research: Solid Earth, v. 105, p. 13159–13177, doi:10.1029/2000JB900060.

McCaffrey, R., Long, M.D., Goldfinger, C., Zwick, P.C., Nabelek, J.L., Johnson, C.K., and Smith, C., 2000, Rotation and plate locking at the Southern Cascadia Subduction Zone: Geophysical Research Letters, v. 27, p. 3117–3120, doi:10.1029/2000GL011768.

Melnick, D., 2016, Rise of the central Andean coast by earthquakes straddling the Moho: Nature Geoscience, v. 9, p. 401–407, doi:10.1038/ngeo2683.

Michel, L., Ehlers, T., and Bendick, R., 2022, Transitions in subduction zone properties align with long-term topographic growth (Cascadia, USA): Earth and Planetary Science Letters, v. 580, p. 117363, doi:10.1016/j.epsl.2021.117363.

Miller, J.R., 2015, The Influence of Bedrock Geology on Knickpoint Development and Channel-Bed Degradation along Downcutting Streams in South-Central Indiana: The Journal of Geology, doi:10.1086/629519.

Mitchell, J.S., Mackay, K.A., Neil, H.L., Mackay, E.J., Pallentin, A., Notman P., 2012. Undersea New Zealand, 1:5,000,000.

Montgomery, D.R., and Brandon, M.T., 2002, Topographic controls on erosion rates in tectonically active mountain ranges: Earth and Planetary Science Letters, v. 201, p. 481–489, doi:10.1016/S0012-821X

Mountjoy, J.J., and Barnes, P.M., 2011, Active upper plate thrust faulting in regions of low plate interface coupling, repeated slow slip events, and coastal uplift: Example from the Hikurangi Margin, New Zealand: Geochemistry, Geophysics, Geosystems, v. 12, doi:10.1029/2010GC003326.

Mountjoy, J., Barnes, P., and Pettinga, J., 2009, Morphostructure and evolution of submarine canyons across an active margin: Cook Strait sector of the Hikurangi Margin, New Zealand: Marine Geology, v. 260, p. 45–68, doi:10.1016/j.margeo.2009.01.006.

National Institute for Water and Atmospheric Research (NIWA), 2015, Virtual Climate Station Network, Average annual rainfall between 1972–2013, Ministry for the Environment.

Nelson, A.R., Hawkes, A.D., Sawai, Y., Horton, B.P., Witter, R.C., Bradley, L.-A., and Cahill, N., 2020, Minimal stratigraphic evidence for coseismic coastal subsidence during 2000 yr of megathrust earthquakes at the central Cascadia subduction zone: Geosphere, v. 17, p. 171–200, doi:10.1130/GES02254.1.

Nicol, A., and Beavan, J., 2003, Shortening of an overriding plate and its implications for slip on a subduction thrust, central Hikurangi Margin, New Zealand: Tectonics, v. 22, doi:10.1029/2003TC001521.

Niemi, N.A., Oskin, M., Burbank, D.W., Heimsath, A.M., and Gabet, E.J., 2005, Effects of bedrock landslides on cosmogenically determined erosion rates: Earth and Planetary Science Letters, v. 237, p. 480–498, doi:10.1016/j.epsl.2005.07.009.

Ninis, D., Little, T., Litchfield, N., Wang, N., Jacobs, K., and Henderson, C.M., 2022, Pleistocene marine terraces of the Wellington south coast – their distribution across multiple active faults at the southern Hikurangi subduction margin, Aotearoa New Zealand: New Zealand Journal of Geology and Geophysics, v. 0, p. 1–22, doi:10.1080/00288306.2021.2011329.

Nodder, S.D., Lamarche, G., Proust, J.-N., and Stirling, M., 2007, Characterizing earthquake recurrence parameters for offshore faults in the low-strain, compressional Kapiti-Manawatu Fault System, New Zealand: Journal of Geophysical Research: Solid Earth, v. 112, doi:10.1029/2007JB005019.

Norabuena, E. et al., 2004, Geodetic and seismic constraints on some seismogenic zone processes in Costa Rica: Seismogenic Processes in Costa Rica: Journal of Geophysical Research: Solid Earth, v. 109, doi:10.1029/2003JB002931.

Paquet, F., Proust, J.-N., Barnes, P., and Pettinga, J.R., 2009, Inner-Forearc Sequence Architecture in Response to Climatic and Tectonic Forcing Since 150 ka: Hawke's Bay, New Zealand: Journal of Sedimentary Research, v. 79, p. 97–124, doi:10.2110/jsr.2009.019.

Pfeiffer, A., Morey, S.M., Karlsson, H.M., Fordham, E.M., and Montgomery, D.R., 2020, Survival of the strong, slow, and dense: Field evidence for rapid, transport-dependent bed material abrasion of heterogeneous source lithology: Earth and Space Science Open Archive, doi:10.1002/essoar.10505262.1.

Pondard, N., and Barnes, P.M., 2010, Structure and paleoearthquake records of active submarine faults, Cook Strait, New Zealand: Implications for fault interactions, stress loading, and seismic hazard: Journal of Geophysical Research: Solid Earth, v. 115, doi:10.1029/2010JB007781.

Portenga, E.W., and Bierman, P.R., 2011, Understanding Earth's eroding surface with ^{10}Be: GSA Today, v. 21, p. 4–10, doi:10.1130/G111A.1.

Reusser, L.J., and Bierman, P.R., 2010, Using meteoric 10Be to track fluvial sand through the Waipaoa River basin, New Zealand: Geology, v. 38, p. 47–50, doi:10.1130/G30395.1.

Reyners, M., 1998, Plate coupling and the hazard of large subduction thrust earthquakes at the Hikurangi subduction zone, New Zealand: New Zealand Journal of Geology and Geophysics, v. 41, p. 343–354, doi:10.1080/00288306.1998.9514815.

Rodgers, D.W., and Little, T.A., 2006, World's largest coseismic strike-slip offset: The 1855 rupture of the Wairarapa Fault, New Zealand, and implications for displacement/length scaling of continental earthquakes: Journal of Geophysical Research: Solid Earth, v. 111, doi:10.1029/2005JB004065.

Savage, J.C., 1983, A dislocation model of strain accumulation and release at a subduction zone: Journal of Geophysical Research: Solid Earth, v. 88, p. 4984–4996, doi:10.1029/JB088iB06p04984.

Schmidt, A.H., Neilson, T.B., Bierman, P.R., Rood, D.H., Ouimet, W.B., and Sosa Gonzalez, V., 2016, Influence of topography and human activity on apparent in situ ^{10}Be-derived erosion rates in Yunnan, SW China: Earth Surface Dynamics, v. 4, p. 819–830, doi:10.5194/esurf-4-819-2016.

Scholz, C., and Small, C., 1997, The effect of seamount subduction on seismic coupling: Geology, v. 25, doi:10.1130/0091-7613

Schwanghart, W., and Kuhn, N.J., 2010, TopoToolbox: A set of Matlab functions for topographic analysis: Environmental Modelling and Software, v. 25, p. 770–781, doi:10.1016/j.envsoft.2009.12.002.

Schwanghart, W., and Scherler, D., 2014, Short Communication: TopoToolbox 2 – MATLAB-based software for topographic analysis and modeling in Earth surface sciences, Earth Surf. Dynam., 2, 1–7, doi: 10.5194/esurf-2-1-2014

Sklar, L., and Dietrich, W., 1998, River Longitudinal Profiles and Bedrock Incision Models: Stream Power and the Influence of Sediment Supply: Washington DC American Geophysical Union Geophysical Monograph Series, v. 107, doi:10.1029/GM107p0237.

Sklar, L., and Dietrich, W., 2008, Implications of the saltation–abrasion bedrock incision model for steady-state river longitudinal profile relief and concavity: Earth Surface Processes and Landforms, v. 33, p. 1129–1151, doi:10.1002/esp.1689.

Tenzer, R., Sirguey, P., Rattenbury, M., and Nicolson, J., 2011, A digital rock density map of New Zealand: Computers & Geosciences, v. 37, p. 1181–1191, doi:10.1016/j.cageo.2010.07.010.

von Blanckenburg, F., 2006, The control mechanisms of erosion and weathering at basin scale from cosmogenic nuclides in river sediment: Earth and Planetary Science Letters, v. 242, p. 224–239, doi:10.1016/j.epsl.2005.06.030.

von Huene, R., Ranero, C.R., and Vannucchi, P., 2004, Generic model of subduction erosion: Geology, v. 32, p. 913, doi:10.1130/G20563.1.

Walcott, R.I., 1987, Geodetic Strain and the Deformational History of the North Island of New Zealand during the Late Cainozoic: Philosophical Transactions of the Royal Society of London. Series A, Mathematical and Physical Sciences, v. 321, p. 163–181.

Wallace, L.M. et al., 2009, Characterizing the seismogenic zone of a major plate boundary subduction thrust: Hikurangi Margin, New Zealand: Geochemistry, Geophysics, Geosystems, v. 10, doi:10.1029/2009GC002610.

Wallace, L.M., 2004, Subduction zone coupling and tectonic block rotations in the North Island, New Zealand: Journal of Geophysical Research, v. 109, p. B12406, doi:10.1029/2004JB003241.

Wallace, L.M., Barnes, P., Beavan, J., Van Dissen, R., Litchfield, N., Mountjoy, J., Langridge, R., Lamarche, G., and Pondard, N., 2012a, The kinematics of a transition from subduction to strike-slip: An example from the central New Zealand plate boundary: Subduction to Strike-slip in New Zealand: Journal of Geophysical Research: Solid Earth, v. 117, p. n/a-n/a, doi:10.1029/2011JB008640.

Wallace, L.M., Beavan, J., Bannister, S., and Williams, C., 2012b, Simultaneous long-term and short-term slow slip events at the Hikurangi subduction margin, New Zealand: Implications for processes that control slow slip event occurrence, duration, and

migration: Hikurangi Margin slow slip events: Journal of Geophysical Research: Solid Earth, v. 117, doi:10.1029/2012JB009489.

Wobus, C., Whipple, K.X., Kirby, E., Snyder, N., Johnson, J., Spyropolou, K., Crosby, B., and Sheehan, D., 2006, Tectonics from topography: Procedures, promise, and pitfalls, in Tectonics, Climate, and Landscape Evolution, Geological Society of America, doi:10.1130/2006.2398(04).

Yanites, B., Tucker, G., and Anderson, R., 2009, Numerical and analytical models of cosmogenic radionuclide dynamics in landslide-dominated drainage basins: Journal of Geophysical Research, v. 114, p. F01007, doi:10.1029/2008JF001088.